Rate-Power Trade-Off in Solar Cell-based

Simultaneous Lightwave Information and Power

Transfer Systems

RATE-POWER TRADE-OFF IN SOLAR CELL-BASED

SIMULTANEOUS LIGHTWAVE INFORMATION AND POWER

TRANSFER SYSTEMS

BY

SAHAND SEPEHRVAND, B.Sc.

A THESIS

SUBMITTED TO THE DEPARTMENT OF ELECTRICAL AND COMPUTER

ENGINEERING

AND THE SCHOOL OF GRADUATE STUDIES

OF MCMASTER UNIVERSITY

IN PARTIAL FULFILMENT OF THE REQUIREMENTS

FOR THE DEGREE OF

MASTER OF APPLIED SCIENCE

Master of Applied Science (2020) McMaster University

(Electrical and Computer Engineering) Hamilton, Ontario, Canada

TITLE: Rate-Power Trade-Off in Solar Cell-based Simultaneous

Lightwave Information and Power Transfer Systems

AUTHOR: Sahand Sepehrvand

B.Sc. (Electrical Engineering),

Amirkabir University of Technology, Tehran, Iran

SUPERVISOR: Dr. Steve Hranilovic

NUMBER OF PAGES: xx, 93

To my parents and my dear sister

Abstract

The Internet-of-Things (IoT) infrastructure is made of uniquely identifiable wireless-enabled smart devices that use the Internet to communicate with each other as well as people, on a large scale. These IoT devices require power to operate, and to communicate with other smart devices. The optical bands have the capacity to provide power and wireless communication to the IoT devices.

Simultaneous lightwave information and power transmission (SLIPT) is a technology through which information and optical power are received simultaneously by the receiver. SLIPT is made possible by solar cell-based SLIPT receivers. In this thesis, for the first time, the trade-off between the achievable data rate and the harvested power in solar cell-based SLIPT systems is quantified and analysed.

It is known that the amount of power harvested using a solar cell is dependent on its operating voltage. By utilizing a realistic electrical model of the solar cells, an expression for the bandwidth and a lower bound on the data rate of a solar cell receiver as function of the operating voltage is derived. Using the dependency of rate and power on the operating voltage, the rate-power trade-off in solar cell based SLIPT receivers are studied in this thesis.

This work proposes a novel solar cell based SLIPT receiver that includes a DC-DC boost converter, which allows control over the operating voltage of the solar

cell. Finally, this thesis proposes an optimization problem to compute the optimum operating voltage for a SLIPT system located indoor where a desired trade-off between the data rate and harvested power can be attained based on the battery state of charge.

Acknowledgements

I would like to express my deep gratitude to Dr. Steve Hranilovic for his guidance and mentorship. His unwavering support and confidence in my abilities allowed me to become a motivated researcher. I am grateful for the opportunity to work under his supervision at McMaster University.

I would also like to thank Dr. Lakshmi Narasimhan from IIT Palakaad for his help.

I would like to thank the administrative team of the Electrical and Computer Engineering Department, especially Cheryl Gies.

I would like to thank my beloved friends, in particular, Sara Imani, Chibueze Ukachi, Amir Hossein Yazdani, Amirreza Salamat, Dale Towey, Ramin Esalat, Pooyan Mehrvarzy, Foad Sohrabi, Mahsa Salmani, Markimba Williams, Khaled Ahmed, Khaqan Majeed, Pouya Hosseini and Hossein Rezaeifar. Thank you for your presence.

I am truly grateful for my parents, who have been the source of inspiration in my life. My achievements, including this Master's degree, would not be possible without their unconditional love and support. There are no words that could express my gratitude toward my parents. Last but not least, I want to thank my dear sister, who is a shining beacon of light in my life.

Symbols and Notation

V DC operating voltage of the solar cell (V)

I Output solar cell current (A)

P Output DC power of the solar cell (V)

I_{sc} Short-circuit current (A)

V_{oc} Open-circuit voltage (V)

I_0 Saturation current of the solar cell (A)

Ir Incident irradiance (W/m^2)

θ Battery charge state (%)

D Duty cycle of DC-DC converter (%)

W Electrical bandwidth of the solar cell (Hz)

R The supported data rate (bit/s)

C_{dl} Depletion capacitance (F)

C_{df} Diffusion capacitance (F)

R_s Series resistance of solar cell (Ω)

R_{sh} Parallel resistance of solar cell (Ω)

r_d Dynamic resistance of the solar cell pn diode (Ω)

Abbreviations

5G   Fifth Generation

Al   Aluminium

AM   Amplitude Modulation

AM   Air Mass

AWGN   Additive White Gaussian Noise

AC   Alternating Current

AP   Access Point

AC   Alternating Current

APD   Avalanche Photodiodes

c-Si   Crystaliline Silicon

D   Duty Cycle

DC   Direct Current

DD   Direct Detection

EH	Energy Harvesting
EHP	Electron Hole Recombination
EHU	Energy Harvesting User
EM	Electromagnetic
EMI	Electromagnetic Interference
FDA	Food and Drug Administration
FM	Frequency Modulation
FOV	Field of View
FF	Fill Factor
GSM	Global System for Mobile Communications
GaAs	Gallium Arsenide
IEEE	Institute of Electrical and Electronics Engineers
IM	Intensity Modulation
IoT	Internet of Things
InGaAsP	Indium Gallium Arsenide Phosphide
IR	Infrared
IU	Information User
LD	Laser Diode

LED	Light Emitting Diode
LOS	Line of Sight
LTI	Linear Time Invariant
MPP	Maxmimum Peak Power
MPPT	Maxmimum Peak Power Tracking
NLOS	Non-Line of Sight
OSHA	Occupational Safety and Health Administration
OWC	Optical Wireless Communications
PD	Photodiode
PDF	Probability Density Function
PM	Phase Modulation
PS	Power Splitting
PSD	Power Spectral Density
QoS	Quality of Service
RF	Radio Frequency
RFID	Radio-Frequency Identification
ROV	Remotely Operated Vehicles
RSS	Received Signal Strength

Rectenna	Rectifying Antenna
Si	Silicon
SLIPT	Simultaneous Lightwave Information and Power Transfer
Sonar	Sound Navigation Ranging
SPD	Spectral Power Density
STC	Standard Test Conditions
SWIPT	Simultaneous Wireless Information and Power Transfer
SINR	Signal to Noise plus Interference Ratio
TOV	Turn On Voltage
TS	Time Splitting
TSw	Time Switching
TDMA	Time Division Multiple Access
US	United States
UL	Underwriters Laboratories
UV	Ultraviolet
V2V	Vehicle to Vehicle
V2X	Vehicle to Everything
VLC	Visible Light Communication

VLP   Visible Light Positioning

VVLC   Vehicular Visible Light Communication

WPT   Wireless power transfer

WSN   Wireless Sensor Networks

Contents

List of Figures

List of Tables

Chapter 1

Introduction

The Internet-of-Things (IoT) infrastructure is made of uniquely identifiable wireless-enabled smart devices that use the Internet to communicate with each other as well as people, on a large scale. These IoT devices require power to operate and to communicate with other smart devices. One of the conditions that enable such an enormous network of interconnected smart devices is one in which the devices are self-sufficient with respect to their energy requirements while maintaining the quality-of-service (QoS). This can be achieved by employing lightweight communication protocols and deployment of low-power transceivers to improve the energy efficiency [1]. The optical bands have the capacity to provide power and wireless communication to the IoT devices.

Visible light communication (VLC) enables wireless communication through visible light. Due to the availability of its vast unlicensed spectrum and immunity to interference with radio frequency (RF) sources, VLC has become a promising physical layer for future IoT networks.
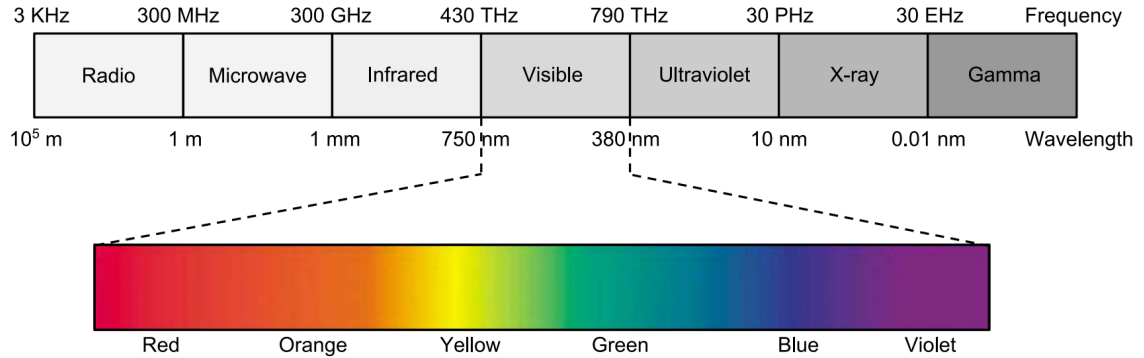
Figure 1.1: The visible light spectrum within the electromagnetic (EM) spectrum [3].

Utilising VLC in an indoor IoT network with solar cell-based receivers has been envisioned to provide an energy-efficient simultaneous lightwave information and power transmission (SLIPT) system. SLIPT is a technology through which the information and optical power are received simultaneously by the solar cell-based receivers [2].

1.1   Visible Light Communication

VLC systems transmit information by modulating the intensity of light within the visible range of wavelengths (375 nm − 780 nm) and is a subset of optical wireless communications (OWC) technologies which also utilise the ultraviolet and infrared range of wavelengths [4, 5]. In VLC, light-emitting diode (LED) luminaires are used as optical transmitters in addition to their primary use, i.e. indoor illumination. LEDs are capable of switching their light intensity at a high rate, and this property is used in VLC to convey information from the LED transmitter to the photodetector receiver while the human eye [6] does not perceive the change in brightness.

LED lighting offers high energy efficiency and high longevity at a low cost, and for

this reason, there has been an exponential growth in the number of LED luminaries in use [4]. According to the US Department of Energy, by the year 2035, about 84% of illumination will be provided by LEDs [7]. The proliferation of LED deployment for indoor illumination along with the design of efficient LED drivers [8] makes VLC a promising solution to the RF "spectrum deficit" [9].

1.1.1 VLC Standards and Commercial Market

Various standards have been published for VLC, aiming to create an extensive adoption while ensuring products and services perform as expected. In December 2011, The Institute of Electrical and Electronics Engineers (IEEE) published the IEEE 802.15.7 standard in which a physical layer (PHY) and a medium access control (MAC) layer are defined for VLC while adhering to eye safety regulations. In addition, since July 2018, the IEEE 802.11bb standard has been actively developing by an IEEE task group, aiming to standardise networked light communications [10]. Multiple companies have been developing commercial VLC products. PureLifi [11], Signify (Philips) [12], Oledcomm [13] and VLNComm [14] have been actively presenting new products for indoor applications.

1.1.2 VLC Applications

VLC offers enormous advantages to many applications in both the indoor and outdoor scenarios. A selection of the VLC applications are named and described in the following.

Indoor Positioning

While the global positioning system (GPS) is widely used for outdoor positioning, GPS fails to operate in indoor scenarios. Using existing VLC-enabled lighting infrastructure in shopping malls and other large outdoor places, visible light positioning (VLP) enables accurate localisation of users equipped with a receiver. Triangulation is a method in which the geometric properties are used to evaluate the position of the receiver based on the distance of the receiver from one or more LED luminaires [15,16]. In [17], the authors used the received signal strength (RSS) to demonstrate VLP with an error of 1.5 cm experimentally. The angle of arrival (AOA) method enables position estimation using the incident angle of beam light from the LED luminaires onto the receiver. The authors of [18] demonstrated AOA positioning with an accuracy of 5 cm. More recently, the 'passive localisation' method was proposed in [19] which uses the channel impulse response (CIR) measurements to locate users without the need to carry a receiver. This approach particularly helps to monitor patients for accidental falls at home, without the use of cameras [20].

In 2012, ByteLight presented an indoor positioning system based on VLC [21]. The company was later acquired by Acuity Brands [22] which released the Atrius Navigator, an end-to-end cloud-based indoor positioning system for mobile devices with an estimation error of 10 cm [23]. The Atrius Navigator not only provides accurate indoor navigation through its smartphone application, but also enables location-based marketing [23].

Philips Lighting, owned by Signify, has employed VLC-enabled LED luminaires to offer indoor positioning with an accuracy of ≈ 10 cm, aiming to improve shopper engagement while analysing the shopper traffic and behaviour data to optimise store

efficiency [24, 25].

High Security Applications

RF signals can penetrate through walls and can, therefore, be subject to eavesdropping. The fact that light cannot go through non-transparent obstacles such as walls enables the design of secure communication links for high-security indoors environment without exposure to eavesdropping [26]. In addition, VLC enables communication to take place in scenarios where RF communication is not possible due to RF jamming [27].

Underwater VLC

Underwater communication is required for remotely operated vehicles (ROV) and communication between divers. Given that RF signals propagating underwater are heavily attenuated (3.5 − 5 dB/m), their range of coverage is limited to a few meters [6, 28]. On the other hand, acoustic (sonar) communication can be used for long-range applications. However, acoustic communication systems suffer from low data rates limited to ≈ 10 Kbps [6] and high latency of a few seconds while being harmful to marine life [29]. Optical signals are capable of supporting data rates in Gbps; hence, VLC for underwater is currently under research for enabling high-speed underwater links. In August 2019, Sonardyne International released a commercial optical communications system named BlueComm 100 which supports a data rate of 5 Mbps for ranges of up to 15 meters. The BlueComm 100 is designed to collect data from underwater instrumentation and to provide live video transmission while operating at 4000 meters underwater [30].
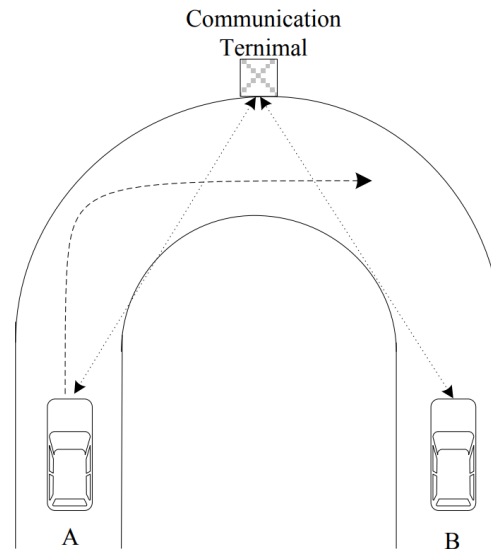
Figure 1.2: VLC-based warning system reduces collision risk at curve lanes [31].

Vehicular VLC

Vehicles can establish VLC links by using their front and back LED lights as VLC transmitter and deploy photodetectors or cameras as receivers. Vehicular VLC (VVLC) can be used for collision avoidance schemes. Consider the scenario depicted in Fig. 1.2 where the drivers have a very narrow view. Suppose that the width of the road supports only one vehicle to pass at any given time. The first vehicle to establish a VLC link with the communication terminal gets the right of way and vehicle B, approaching from the other direction, receives a warning stop signal [31]. In addition, VVLC has the potential to deliver the fifth-generation (5G) vehicle-to-everything (V2X) concepts such as forward collision warning and platooning [32].

EMI-sensitive environments

VLC links do not interfere with radio signals and are suitable to be deployed in aircraft cabins, hospital rooms and petrochemical plants, where electromagnetic interference (EMI) is a potential hazard and often prohibited [6].

1.2   Power Harvesting

Power harvesting (also referred to as energy harvesting) is the process of capturing energy from the ambient energy sources such as sunlight, vibration and heat, per unit time and converting them into electrical power to feed small electronic devices [33]. These electronic devices may include wireless IoT devices [1] or wearable electronic devices [34]. Other sources of ambient energy include the indoor artificial lighting which can be harvested using solar cells [35] and the existing electromagnetic waves of the radio frequency (RF) range which can be harvested using a high gain antenna [36].

The IoT infrastructure is made of uniquely identifiable wireless-enabled smart devices use the Internet to communicate with each other as well as people, on a large scale. One of the conditions that enable such an enormous network of inter-connected smart devices is one in which the devices are self-sufficient with respect to their energy requirements while maintaining the quality-of-service (QoS). This can be achieved by employing lightweight communication protocols and deployment of low-power transceivers to improve the energy efficiency [1]. The motivation behind energy scavenging is to supply power to such IoT devices with small power requirements, $\approx$ 10 mW [37], in order to elongate their battery life, and ultimately, to reach self-sufficiency.

In addition, Harvest-Use architectures, in which there is no power storage unit, the energy is harvested just in time to be used. These systems typically harvest mechanical work such as a push of a key button and using it to deform a piezoelectric material and converting the energy to electrical voltage [33].

Table 1.1 displays common ambient energy sources sorted according to their available power density. Solar cells are used to harvest sunlight and indoor lighting according to the photovoltaic effect. In order to create power from vibrations, the piezoelectric effect is exploited which involves generation of electrical voltage or current from mechanical vibrations. Power can be harvested from thermal sources by using thermoelectric devices which create electrical voltage from the temperature difference in the environment. Lastly, ambient RF energy offers the lowest power density and is harvested using the rectenna design mentioned in Sec. 1.3.2. As it is clearly apparent, the solar light and indoor lighting have the highest power density among others and are studied in this thesis. Solar power conversion efficiency is further discussed in Sec. 3.3.2.

1.3 Wireless Power Transfer

Wireless power transfer (WPT) was first introduced by Nikola Tesla. While his dream of a "wirelessly powered world" was never realised to the full extent, he is yet regarded as a pioneer of WPT [38, 39]. In a WPT system, electrical power is transmitted to the receiver in a wireless manner, where the power is then converted to direct current (DC) power. By producing an oscillating electromagnetic field, power is transmitted through space. WPT architectures fall within two main categories: near-field and far-field [34, 40].

Source	Power Density	Advantages	Disadvantages
Sunlight [33]	100 mW/cm^2	Ambient source, high power density, high output voltage	Sensitive structure Only available during the day
Indoor Lighting [35]	$0.538^1 - 5.38^2$ mW/cm^2	Controllable, SLIPT capable	Low power density, Low output voltage
Vibration [36]	200 µW/cm^3	Controllable light weight	Activity dependant, large area required, variable output
Thermal [41]	50 µW/cm^2	Ambient source, scalable	Efficient heat sinking required, inconsistant availability
RF [41]	1 µW/cm^2	Ample in urban areas, enables mobility	Low power density, limited in rural areas, distance-dependant

Table 1.1: Available sources for power harvesting

1.3.1   Near-Field WPT

Near-field WPT applications include contactless smart cards, wireless smartphone charging and passive radio frequency identification (RFID) tags. The aforementioned applications are based on the resonant inductive coupling phenomenon which was first discovered by Tesla, allowing for application with an effective range of a few centimetres. [42, 43].

---

[1]Illumination for an office.
[2]Illumination for difficult visual tasks.

1.3.2   Far-Field WPT

Far-field WPT systems transmit power via electromagnetic radiation. Effective long-range applications are limited to RF/microwave and optical (laser beam) propagation as indicated in Fig. 1.1 [40]. About 70 years after Tesla's experiments, William C. Brown developed the first rectifying antenna (rectenna) which was used to receive and rectify microwaves and produce a DC output power [44]. Applications of RF WPT include wireless sensor networks, which consist of sensors with low power requirements [43].

Since 2014, the company Wi-Charge has demonstrated several prototypes of far-field wireless power transmission via focused infrared (IR) laser beams. Given the safety concerns regarding IR laser beams, the system is designed such that a narrow beam is propagated to the receiver only when a line-of-sight (LoS) orientation exists between the IR transmitter and the photovoltaic unit in the receiving end. In 2019, the company announced that its LIGHTS-3W system has earned the Underwriters Laboratories (UL) certificate along with the Food and Drug Administration (FDA) approval and is compliant with the Occupational Safety and Health Administration (OSHA) [45].

It is often the case that Far-field WPT is confused with power harvesting in the literature. It is important to note that while power harvesting refers to the collection of power from the *ambient* sources of the energy, in WPT systems, the power is transmitted and often pointed directly at the receiver for the sole purpose of power delivery. As long as the existing RF sources such as GSM and WiFi signals and the light energy from the artificial lighting infrastructures operate within their nominal output power levels, they are regarded as ambient resources, and the technology is

categorised an energy harvesting rather than WPT.

In the previous section, WPT was reviewed for near-field and far-field scenarios. Given the unpredictable nature of ambient energy sources described in section 1.2, the reliable power transfer offered by WPT architectures make them a suitable technology to power IoT devices and sensors. While RF and optical waves proved to be the most effective for far-field communication, these technologies have been extensively studied for another application: wireless communications. Hence, the coexistence of WPT and wireless (RF and Optical) communication is of great interest to the research community.

1.4 Simultaneous Wireless Information and Power Transfer

Simultaneous wireless information and power transfer (SWIPT) is referred to a system in which RF antennas receive information and power from an RF signal of a specific band of frequencies. SWIPT has been extensively studied, and many system models for wireless sensor networks (WSN) have been investigated [47]. These small sensors are located in hazardous or distant spots such that changing batteries or providing wired power source is rather difficult. Hence, SWIPT enabled WSN is a promising solution to this problem [47]. In SWIPT systems, the transmitted RF signal is converted into DC power via the rectenna architecture. In SWIPT systems, the received signal is typically subject to time switching (TSw) or power splitting (PS) [48, 49].

(a)

(b)
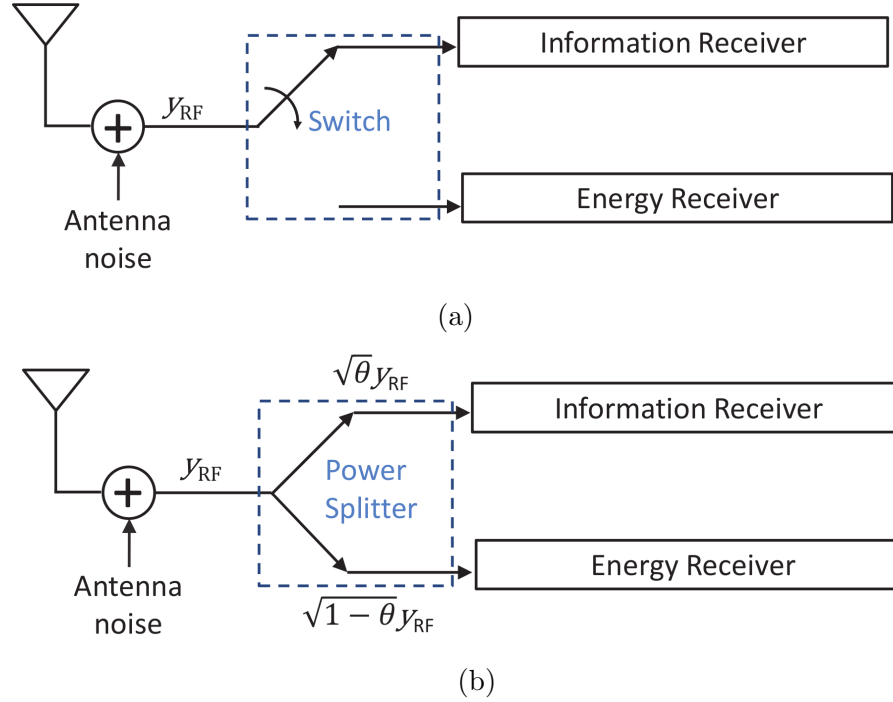
Figure 1.3: SWIPT Receiever Architecture, (a) Time switching, (b) Power splitting. [46]

In the TSw architecture, the receiver switches between power collection and information reception in a given time interval. While the TSw architecture is simple to implement, perfect synchronisation has to be established between the transmitter and the receiver while requiring a more complex receiver compares to the TSw method [46].

In PS architecture, the receiver is able to receive information and power in a truly simultaneous manner. As it is shown in Fig. 1.3b, the input signal y_{rf} is split into $\sqrt{\theta}Y_{RF}$ and $\sqrt{1-\theta}Y_{RF}$ components for the information receiver and the energy receiver, respectively. The power splitting method allows for continuous information decoding and power reception [46].

Current research directions in SWIPT includes the design of high gain antennas that operate in a wide range of frequencies. Since the sensitivity of SWIPT receivers are lower than ordinary antennas, and this does not allow the deployment of SWIPT in a certain communications system. Lastly, RF powered systems require a firm power constraint and such systems can only support low complexity algorithms with relatively low computation power requirements. Hence, another research direction is to design low complexity channel coding and modulation schemes for RF powered communication networks [47].

1.5   Simultaneous Lightwave Information and Power Transfer

The optical counterpart of SWIPT, simultaneous lightwave information and power transfer (SLIPT), coined by Diamantoulakis *et al.* [50], refers to a system in which information and power are transferred and received through optical (IR and visible light) intensity signals. In this scenario, the LEDs luminaires are used for three purposes: illumination of environment, information transmission and power transmission.

Solar cells are one potential device to realise SLIPT, as the optical counterpart of the rectenna in SWIPT system. While the potential use of solar cells as optical detectors was first analysed in [51], the first receiver circuit was designed in [52] which experimentally demonstrated simultaneous power and information reception with a data rate of 11.84 Mbps[3].

SLIPT systems are realised by using solar cells as optical receivers as well as their

---

[3]The harvested power was not reported
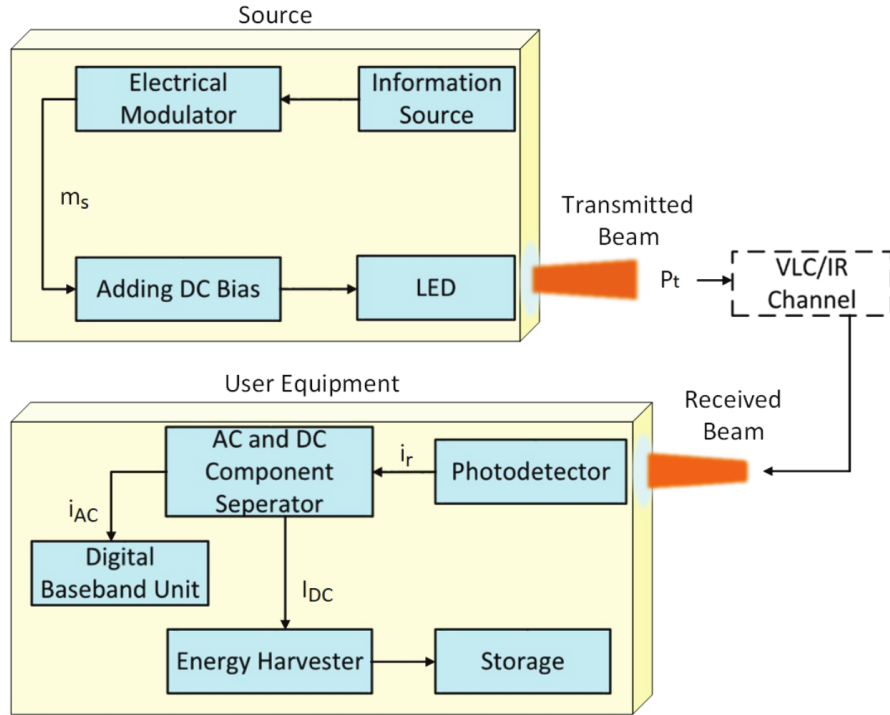
Figure 1.4: SLIPT transmitter and receiver model [46]

primary energy conversion function. Fig. 1.4 shows the SLIPT transceiver design [46], in which a DC bias component is added to the AC signal m_s at the transmitter. At the receiver, the DC and AC components are directly split for power harvesting and information reception, respectively. The DC bias is an important variable in SLIPT systems as it can be used to control the illumination of the room and the power density incident on the solar cell receiver.

Inspired by the TSw in SWIPT, time splitting (TS) is a mode of operation in which the SLIPT receiver performs either power collection or information reception at specific time intervals [2, 50]. Consider T, as illustrated in Fig. 1.5, as the block transmission time in seconds. For the first αT seconds (phase 1), the receiver uses the AC component of the received optical signal for information reception and the
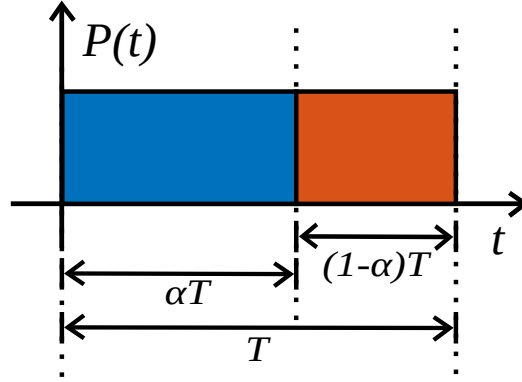
Figure 1.5: Time Splitting Signaling

remaining $(1 - \alpha) T$ seconds (phase 2) are used for power collection, where $0 \leq \alpha \leq 1$.
In phase 1, the signal-to-noise plus interference ratio (SINR) is maximised to optimise
information reception, and in phase 2, the AC component of the sent signal is set to
zero while DC bias is maximised to facilitate power collection. In addition to TS, the
authors also present adjustable field-of-view (FoV) in [50], which is achieved by using
liquid crystal lenses which enable tuning of the FoV to maximise SINR in phase 2.
DC bias optimisation is also considered to complement the adjustable FoV method.

Another approach to meet the QoS requirements of the users in SLIPT systems
is to control the illumination level. In [53], an indoor scenario with multiple LED
transmitters (access points) consisting of units that only harvested energy (EHU)
and units that only received information (IU) was considered. The optimal DC bias
vector for j access points (APs) was found to maximise the sum-rate and the total
power harvested subject to QoS constraints (minimum data rate IUs and minimum
energy harvesting for EHUs) for k users. In [54,55], an outdoor scenario is considered
with a single transmitter, in which the transmission frame of T seconds is divided
between the k users. Resource allocation problems are defined as an optimisation of
the spectral efficiency for the time division multiple access (TDMA) scheme with an

unequal time slot and power allocation between users.

In [56], the authors implemented an outdoor SLIPT system in which the rooftop solar panels equipped with maximum peak power tracking (MPPT) harvested solar power while receiving information via an eye-safe beam of laser light incident from a lighthouse at a distance of 30 meters. The supported data rate was 5 Mbps.

1.5.1   SLIPT Challenges

Solar cells are fundamentally designed for outdoor power harvesting from the sunlight; hence, they are not optimised for communication applications and exhibit large capacitance and subsequently, a small bandwidth.

In addition, the power density of an indoor environment is limited. In the previous section, several ideas we presented which improved the spectral efficiency, data rate and the amount of harvested power in single-cell and multi-cell scenarios. These strategies could be categorised into two groups:

1. Transmission Adjustment

   - Time splitting [2, 50]

   - DC bias optimisation [2]

   - TDMA time slot optimisation [54, 55]

2. Reception Adjustment

   - Maximum peak power tracking [56]

   - FoV adjustment [50]

Although the resource allocation problems enable the optimal DC bias to be found for maximum rate and power collection, the optimal DC bias is likely to violate the illumination requirements of the indoor environments. Another strategy for adjusting transmission would be to find the optimal location for the receivers, subject to a given set of QoS requirements [57].

1.6   Thesis Contributions

This thesis describes and proposes a novel adaptive-SLIPT solar cell-based receiver. While earlier approaches mimicked TS and PS from SWIPT, this work considers the fundamental electrical characteristics of solar cells in quantifying a trade-off between power and data rate. This new approach enables the communication rate and the output power of the receiver to be optimised based on the battery state of the receiver [58].

All previous approaches to SLIPT assume a constant, known bandwidth for the solar cell receiver. In this thesis, a detailed derivation of the solar cell's voltage-dependent bandwidth is derived from a small signal (AC) model of the receiver, showing that the bandwidth is a function of the DC terminal characteristics of the solar cell. The bandwidth expression is then used to derive a tight lower bound on the channel capacity as a function of the solar cell's operating voltage, given the signalling design for the LED transmitters. Given that the solar cell's operating voltage determines its output power, using the lower bound on the data rate, the inherent rate-power trade-off for the solar cell-based receiver is quantified for the first time.

The proposed receiver is equipped with a DC-DC boost converter that is used to

control the operating voltage of the solar cell, hence enabling the desired trade-off to be attained based on the battery state information.

Finally, a system design problem is formulated as an optimisation to find the optimum solar cell DC operating voltage to obtain a trade-off between rate and power for a given battery charge state and background irradiance. The two proposed optimisation objectives are compared and analysed based on optimal results.

1.7   Thesis Structure

Chapter 2 presents background on indoor VLC systems. The intensity modulation-direct detection (IM-DD) optical channel model is described for the line-of-sight (LoS) orientation as well as the non-line-of-sight component. The signalling scheme, along with the solar cell parameters for the MATLAB simulations of the rest of the thesis, is presented.

Chapter 3 reviews the solar cell fundamentals, including the DC equivalent circuit. The I-V and P-V plots of the solar cell simulation on MATLAB are displayed to show the effect of irradiance on the cell's output characteristics. Key defining characteristics of the solar cell, such as the fill factor (FF) and efficiency, are reviewed. The theoretical limits on solar cell efficiency are discussed for both single-junction and multi-junction solar cells. The maximum peak power tracking method is reviewed as a method to maximise the cell's output power. Finally, the AC equivalent circuit of the solar cell is studied and the expression for the two capacitances, namely diffusion and depletion, is derived from the semiconductor basics of the pn junction. By plotting the C-V characteristics of the solar cell capacitance, the contribution of each capacitance is indicated.

Chapter 4 presents the novel adaptive solar cell-based receiver. The DC and AC equivalent circuits of the adaptive-SLIPT receiver are presented, and an analytical expression for the proposed receiver is derived as a function of the cell's operating voltage. The plot of the simulated solar cell's bandwidth vs cell's operating voltage is shown to demonstrate that the bandwidth is not dependant on the irradiance.

Chapter 5 defines the rate-power trade-off for the proposed receiver. A tight lower bound on the channel capacity is derived for the signalling design demonstrated in chapter 2. R-V plots are plotted to demonstrate the dependency of the supported rate on the irradiance level. The rate-power trade-off is demonstrated through P-R plots of the solar cell simulation on MATLAB. Finally, a system design problem is formulated as the optimisation of two objectives, namely arithmetic mean and geometric mean, to find the optimal operating voltage of the adaptive SLIPT receiver for any given irradiance and battery charge state. The optimal operating voltage then numerically computed and plotted as a function of the battery charge, for different irradiance levels.

Finally, Chapter 6 concludes the key findings of this thesis and suggests potential extensions of this work.

Chapter 2

System Model

In order to design efficient receivers for any communication system, it is essential to understand and model the behaviour of the channel for different scenarios. In this chapter, the VLC channel model is studied for different communication links between the transmitter and the receiver. The VLC transmitter and receiver devices are reviewed. The chapter moves on to derive the line-of-sight DC channel gain for the indoor VLC environment. Finally, the SLIPT system model considered in this thesis, the signalling for SLIPT systems along with the simulation parameters, are explained.

2.1   Optical IM-DD Channel

The optical wireless channel is fundamentally different from the RF channels. In the RF domain, the *information* is carried by the amplitude (AM), the phase (PM), the frequency (FM) of the carrying sinusoidal or other generalisation of these techniques.
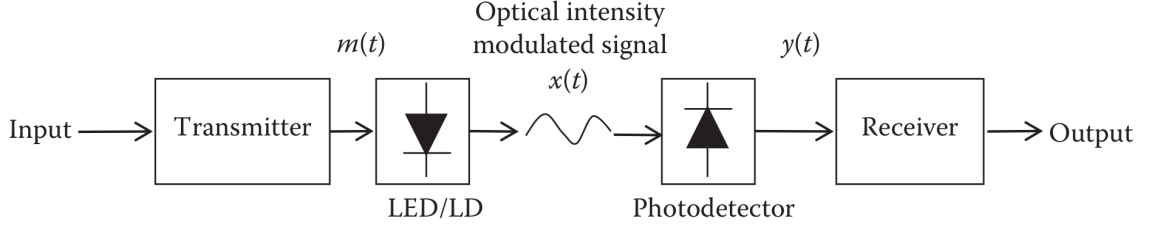
Figure 2.1: Block diagram of the optical IM-DD channel [59]

In contrast, in the optical domain, the *information* is carried by the instantaneous optical power of the optical transmitter, which can be LEDs or laser diodes (LDs). This is referred to as intensity modulation (IM). At the receiver, the photodetector, with an area of order $\approx 10^4 \lambda$, produces a current proportional to the incident optical power. This is referred to as direct detection (DD). Hence, the channel considered in this work is referred to as the IM-DD channel, as shown in Fig. 2.1 [60, 61].

2.1.1 LED Transmitters

An LED is a pn junction diode often made from direct band gap semiconductor materials such as GaAs. In these devices, the electron-hole pair (EHP) recombination takes place, resulting in the emission of a photon from the pn junction of the LED. The output spectra of the LEDs depends on the semiconductor material, the doping concentration and the structure of the device. In addition, the temperature of the device also scales and shifts the output spectrum of the LEDs, as shown in Fig. 2.2(a). The current through an LED is given by the Shockley equation

$$I_{LED} = I_s \left(e^{\frac{qV_{LED}}{kT}} - 1 \right) \simeq I_s e^{\frac{qV_{LED}}{kT}}, \qquad (2.1.1)$$
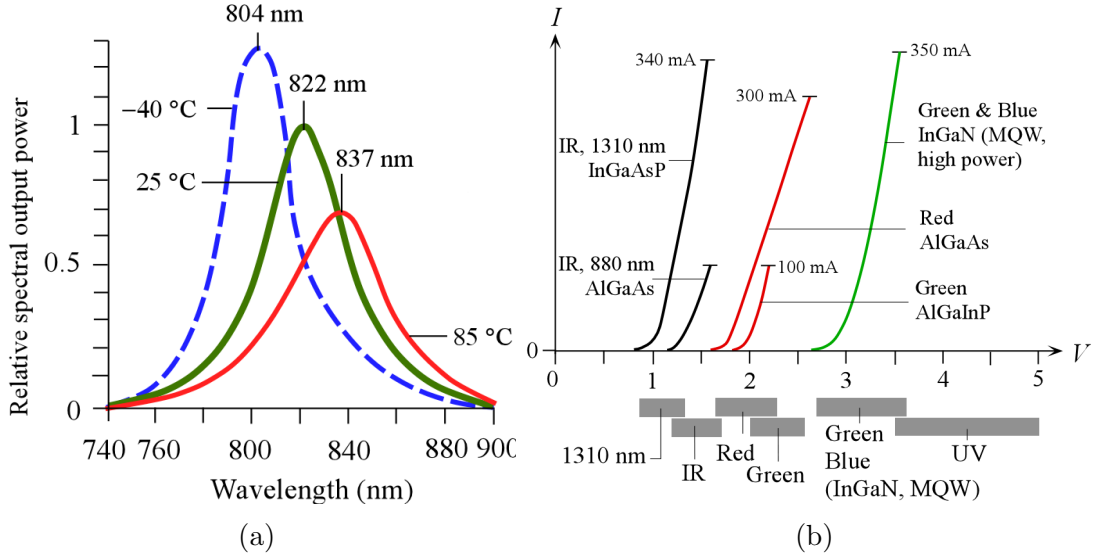
Figure 2.2: (a) I-V characteristics of LEDs of different colours, (b) Variation of the relative spectral output power of the AlGaAs IR LED with temperature [62].

where k is the Boltzmann constant and T is the Temperature in Kelvin and I_0 is the reverse saturation current. It is the temperature dependency of I_0 that explains the scaling and shifting effects of temperature variation in Fig. 2.2(a). Fig. 2.2(b) displays I-V plots of IR and coloured LEDs. The voltage beyond which the current starts increasing in an exponential manner is referred as the turn on voltage (TOV) of the LED. In addition to the non-linear relationship of the LED current I_{LED} with its voltage V_{LED}, the emitted optical power P_{LED} of the LED is also a non-linear function of I_{LED}. Fig. 2.3 demonstrates this non-linearity for a commercial white LED, manufactured by Everlight Electronics [63]. P_{LED} can be expressed by a Taylor series approximation in terms of the driving current of the LED

$$P_{LED} = \sum_{n=0}^{N} \alpha_n (I_{LED} - I_{DC})^n, \qquad (2.1.2)$$
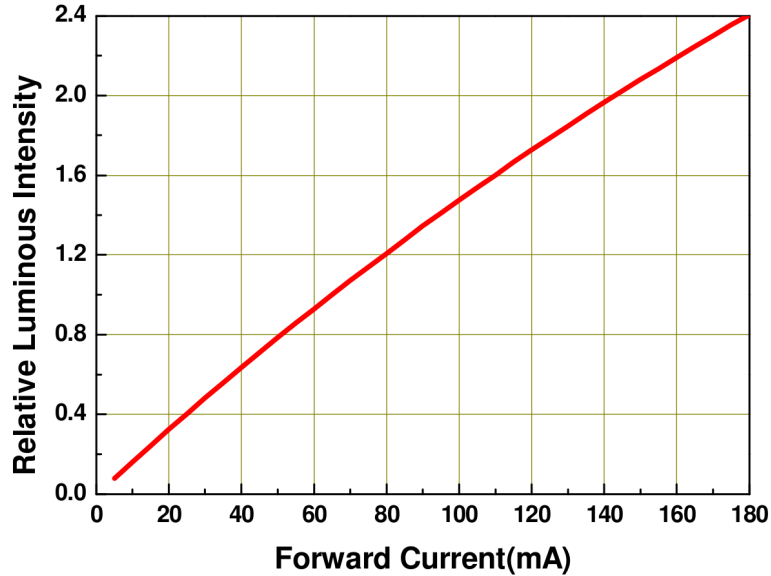
Figure 2.3: Non-linear relationship between the light intensity and LED current for a commercial white LED [63].

where α_n is the coefficient of the nth order of the polynomial and I_{DC} is the DC bias current of the LED [64, 65].

White LEDs are the main type of LEDs used for indoor illumination. Given that white light is composed of a mixture of other colours, it cannot be produced directly by an LED [66]. There are two methods employed to create white light from LEDs. The first approach is to mix the red, green and blue (RGB) colours to render white light. However, this method of white light production is not favoured since the efficiency of the green LED is significantly lower than red and blue, which limits the overall efficiency of the LED. In addition, the efficiencies of red, green and blue LEDs change over time, and this change occurs at a different rate for each colour; hence the rendered quality deteriorates over time [67]. The second method of producing white light is photoluminescence: light is emitted from a material, termed
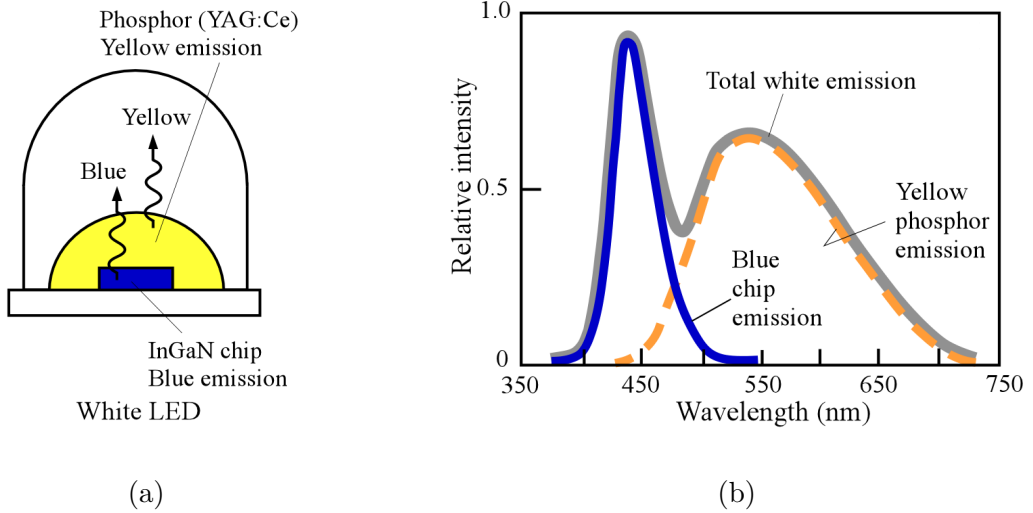
Figure 2.4: White LEDs: (a) RGB LED, (b) Spectral distribution of white LED [62].

a 'phosphor', that has been initially excited by light of higher frequency than emitted light. Fig. 2.4(a) shows a InGaN LED of blue light, with a thin coating of phosphor. The blue light emitted is initially absorbed by the phosphor and is then re-emitted as yellow light [62]. The coating is thin enough for a fraction of the blue light to transmit through the LED, and hence, the resultant emission is white light [68]. The spectral distributions of the blue light, yellow light and the resultant white light are displayed in Fig. 2.4(b). Commercial white LEDs have similar spectral distribution characteristics [69].

Note that in the case of an RGB LED, there would be three distinct peaks for each LED, resulting in a poor white colour rendering [68].

2.1.2   Photodiodes

Photodiodes are solid sates devices that enable direct detection by producing a photo-current I_{ph} proportional to the incident optical power on their surface area, P_0 according to

$$I_{ph} = RP_0, \tag{2.1.3}$$

where R is the responsivity of the photodiode and has units of Amperes per Watt $\left(\frac{A}{W}\right)$. Photodiodes require a constant DC power supply to create a reverse bias that enables the photodiode to operate [62]. The photodiode responsivity R is defined as

$$R = \frac{\text{Photocurrent (A)}}{\text{Incident optical power (W)}} = \frac{I_{ph}}{P_0} = \eta_e \frac{q}{h\nu} = \eta_e \frac{q\lambda}{hc}, \tag{2.1.4}$$

where η_e is the quantum efficiency (EQ) of the photodiode, q is the charge of an electron, h is the plank constant, and c is the speed of light. As it is clear from (2.1.4), R is dependant on the wavelength of the incident light. The R-λ characteristics repre-sent the spectral response of the photodiode and are provided by the manufacturers. The R-λ characteristics of conventional photodiodes, covering the visible, UV and IR range of wavelengths, are displayed in Fig. 2.5. Note that η_e is also dependant on λ. Common photodiodes used are pn, pin and avalanche photodiodes (APD) which differ in terms of the semiconductor material and the solid-state architecture. Table 2.1 displays the typical performance characteristic parameters of pn, pin and APD photodiodes. The disadvantage of pn photodiodes is that they offer inadequate bandwidth for high frequency modulation. The improved pin photodiodes offer a higher bandwidth with respect to pn photodiodes, as shown in Table 2.1. APDs are
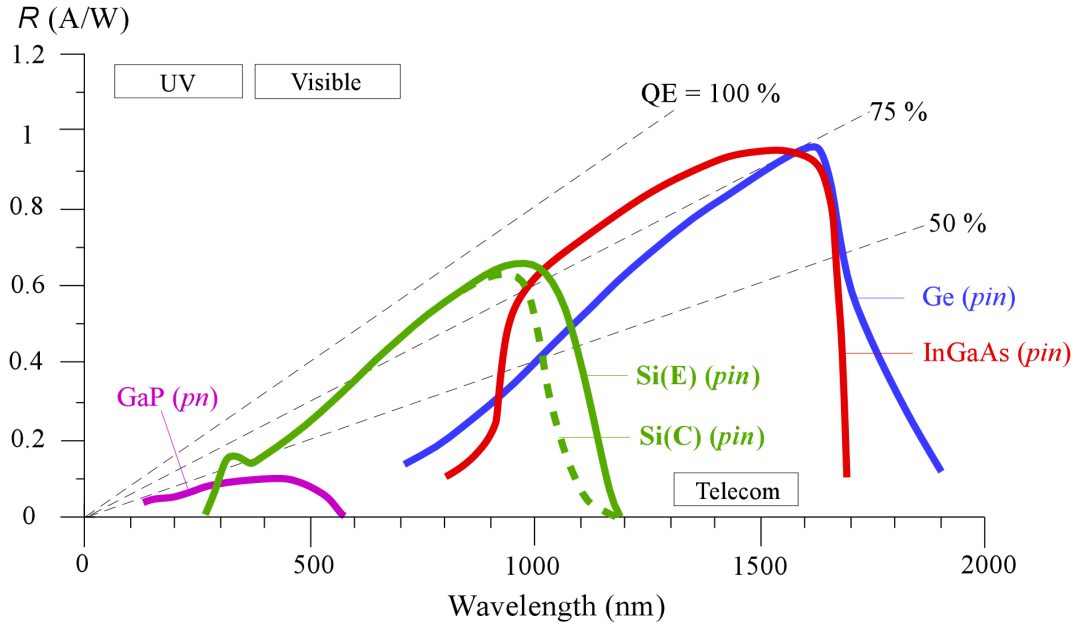
Figure 2.5: Spectral response of GaP(pn), Si(pn), Ge(pin) and InGaAs(pin) photodiodes. The dashed lines represent the responsivity for QE = 100% (ideal photodiode), QE = 75% and QE = 50% [62]

popular in optical communications because of their internal gain mechanism leading to large gain values shown in Table 2.1, while offering a very high speed (bandwidth). Note that as the upper bound of λ_{range} of the photodiodes increases, the responsivity $R_{\lambda_{peak}}$ also increases.

Solar Cells as Optical Receivers

In this work, solar cells are employed in a SLIPT system to detect optical signals while their primary purpose is to convert optical power to electrical current. While photodiodes have been used to detect high-speed optical intensity signals for the past decades, they require power to operate [70]. In contrast, solar cells have the capability to produce power while functioning as optical receivers [71]. While both devices

Photodiode	λ_{range} (nm)	$R_{\lambda_{peak}}$ (A/W)	Gain	Features
Si pn	200-1100	0.5-0.6	< 1	Inexpensive
Si pin	300-1100	0.5-0.6	< 1	Faster than pn
Si APD	400-1100	0.4-0.6	$10 - 10^3$	Fast, high gain
GaAs pin	570-870	0.4-0.5	< 1	High speed
GaAsP pn	150-750	0.2-0.4	< 1	UV to Visible
InGaAs APD	800-1700	0.7-0.95	$10 - 20$	High speed, high gain

Table 2.1: Typical performance parameters for pn, pin and APD-type photodiodes for Si, GaAs, GaAsP and InGaAs [70].

ordinarily consist of a pn junction, the operation of a solar cell is fundamentally different from photodiodes; as presented in Sec. 3.7, in solar cells, the pn junction operates under forward bias. Whereas, in the case of a photodiode, the pn junction operates under reverse bias. For this reason, solar cells exhibit a higher capacitance, which leads to a smaller bandwidth compared to the photodiodes. As a result, the supported rate of communication using a solar cell-based receiver is limited by solar cell bandwidth.

2.2   Channel Model

The communication system displayed in Fig. 2.1 is modelled as a baseband linear, time-invariant (LTI) system as shown in Fig. 2.6. The VLC channel model is given
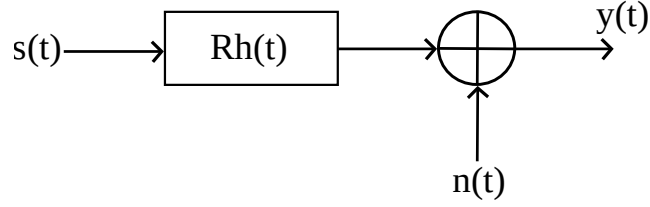
Figure 2.6: The equivalent baseband model of the IM-DD channel [72].

by

$$y(t) = Rs(t) \circledast h(t) + n(t), \tag{2.2.1}$$

where $y(t)$ is the received electrical current (A), $s(t)$ is the instantaneous power emitted from the transmitter (W), R is the responsivity of the photodiode in units of $\left(\frac{A}{W}\right)$, $h(t)$ is the channel impulse response (CIR), $n(t)$ is the zero-mean signal independent additive white Gaussian noise of the VLC channel (A) and $\circledast$ denotes the convolution operation in an LTI system. While the channel model presented in (2.2.1) is linear filter with an additive white gaussian noise (AWGN), the OWC channel and therefore the VLC channel differ from their radio counterpart in two main constraints for optical communication. The first constraint is that the channel input must be non-negative, as it represent the instantaneous optical power, hence

$$s(t) \geq 0. \tag{2.2.2}$$

The second constraint arises due to the eye safety regulation [6] which implies a limit P_{max} on the average optical power transmitted P_t, defined as

$$P_t = \lim_{T \to \infty} \frac{1}{2T} \int_{-T}^{T} s(t) \, dt \tag{2.2.3}$$
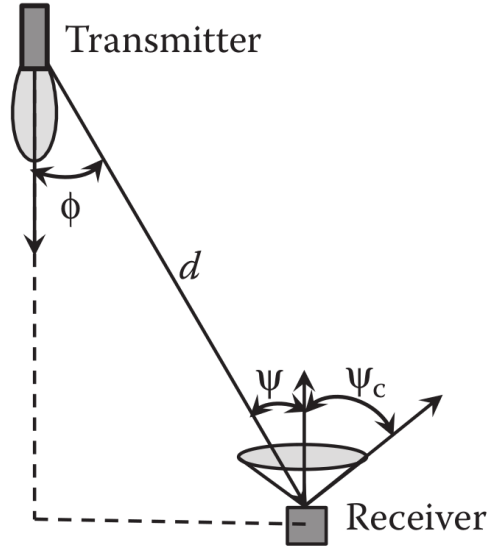
Figure 2.7: The line-of-sight (LOS) VLC link [72]

$$P_t \leq P_{\max} \qquad (2.2.4)$$

The average optical power received is attenuated by the channel, and is defined as

$$P = H\left(0\right) P_t, \qquad (2.2.5)$$

where $H(0)$ is the optical channel DC gain defined as

$$H\left(0\right) = H\left(f\right)|_{f=0} = \int_{-\infty}^{\infty} h\left(t\right) e^{-2\pi f t} dt \bigg|_{f=0} = \int_{-\infty}^{\infty} h\left(t\right) dt \qquad (2.2.6)$$

2.2.1   Channel Impulse Response

The following analysis is largely based on the work of [60,72]. For an indoor scenario, there are two main types of links between the transmitter and the receiver: The line-of-sight (LOS) and the non-line-of-sight (NLOS.) The LOS link, shown in Fig. 2.7, is defined as a link in which the light beam forms a straight line from the transmitter to the receiver. In contrast, the NLOS link consists of light components which are reflected off reflective surfaces such as the wall before becoming incident upon the receiver.

LoS DC Channel Gain

Consider a LOS link as shown in Fig. 2.7. For a photodiode with a physical area of A, equipped with an optical concentrator with gain of $g\left(\varphi\right)$ gain and an optical filter with signal transmission $T_s\left(\varphi\right)$, the effective is given by

$$
A_{eff}\left(\varphi\right) = \begin{cases} AT_s\left(\varphi\right)g\left(\varphi\right)\cos\left(\varphi\right), & 0 \leq \varphi \leq \varphi_c \\ 0, & 0 \geq \varphi_c \end{cases}
\tag{2.2.7}
$$

where φ is the angle of incidence with respect to the normal vector of the photodiode plane, φ_c is the field of view (FoV) of the concentrator also reffered to as the semiangle. Note that the signal transmission of $T_s\left(\varphi\right)$ is averaged over all incident wavelengths within the range of the filter. The expression for $g\left(\varphi\right)$ with an internal refractive index of n is given by

$$
g\left(\varphi\right) = \begin{cases} \frac{n^2}{\sin^2\left(\varphi_x\right)}, & 0 \leq \varphi \leq \varphi_c \\ 0, & 0 \geq \varphi_c \end{cases}
\tag{2.2.8}
$$

The emitted radiation pattern is symmetric with respect to the vertical axis of the transmitter, with a radiant intensity of $p_t R_0 (\phi)$ where $R_0 (\phi)$ is the normalised radiation pattern. Let Ir denote the power incident on a given surface per unit area or the irradiance. The irradiance $Ir (d, \phi)$ incident upon the receiver at distance d is then given by

$$Ir (d, \phi) = \frac{p_t R_0 (\phi)}{d^2} \qquad \left(\frac{\text{W}}{\text{m}^2} \right), \tag{2.2.9}$$

and the received power is given by

$$P = Ir (d, \phi) A_{eff} (\varphi) = \frac{p_t R_0 (\phi)}{d^2} A_{eff} (\varphi). \tag{2.2.10}$$

The channel DC gain $H(0)$ in (2.2.5) is obtained using (2.2.7):

$$H(0)_{LOS} = \begin{cases} \frac{A}{d^2} R_0 (\phi) T_s (\varphi) g (\varphi) \cos (\varphi), & 0 \leq \varphi \leq \varphi_c \\ 0, & 0 \geq \varphi_c \end{cases} \tag{2.2.11}$$

The radiation pattern $R_0 (\phi)$ can be modeled as a generalised Lambertian pattern of order m [73]

$$R_0 (\phi) = \frac{m + 1}{2\pi} \cos^m (\phi), \tag{2.2.12}$$

where m is the Lambertian order

$$m = \frac{- \ln 2}{\ln \{ \cos (\Phi_{1/2}) \}}. \tag{2.2.13}$$

The channel DC gain with an LED transmitter for the LOS is expressed as

$$
H(0)_{LOS} = \begin{cases} \frac{A(m+1)}{2\pi d^2}\cos^m(\phi) \, T_s(\varphi) \, g(\varphi) \cos(\varphi), & 0 \leq \varphi \leq \varphi_c \\ \\ 0, & 0 \geq \varphi_c. \end{cases} \tag{2.2.14}
$$

The channel impulse response could be expressed with a delta Dirac function as follows:

$$
h(t) = \frac{A(m+1)}{2\pi d^2}\cos^m(\phi) \, T_s(\varphi) \, g(\varphi) \cos(\varphi) \, \delta\left(t - \frac{d}{c}\right) \tag{2.2.15}
$$

where the delta function is delayed by $\frac{d}{c}$ which is the time it takes for light to travel the distance d from the transmitter to the receiver in the LoS link.

2.3   SLIPT System Model

In this thesis, we consider the downlink connection of an indoor VLC based IoT system as shown in Fig. 2.8. This system consists of LED luminaires that are fixed on the ceiling of the room and solar-cell based sensors inside the room.

In the downlink, the LED luminaires transmit data to the IoT sensors through the VLC channel. Traditionally, photodiodes are used to detect the instantaneous intensity of the received lightwave. Since the photodiodes cannot harvest photovoltaic energy and require an applied bias to operate, the energy efficiency of the IoT devices can be maximised by employing solar cells. Thus, in this setup, the IoT devices employ a solar cell to receive data and power simultaneously.
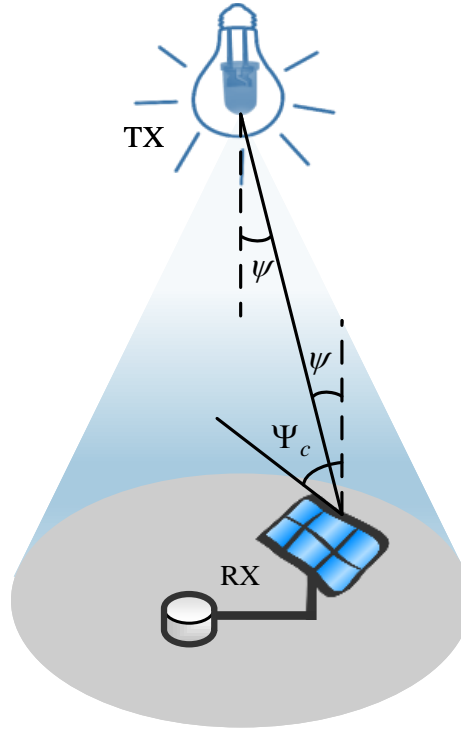
Figure 2.8: Indoors VLC downlink system setup

2.3.1 Signaling

The LED luminaires transmit a non-negative signal which constitutes of a zero-mean signal (referred to as the AC component) and a constant non-zero signal (referred to as the DC component); this is illustrated in Fig. 2.9. Let $s(t)$ be the signal transmitted through intensity modulation, such that

$$s(t) = x(t) + P_0, \tag{2.3.1}$$

where P_0 is the DC component that ensures the transmitted signal is non-negative and $x(t)$ is the AC component. Let A denote the peak-to-peak amplitude of $x(t)$

$$A = \max\{x(t)\} - \min\{x(t)\}. \tag{2.3.2}$$
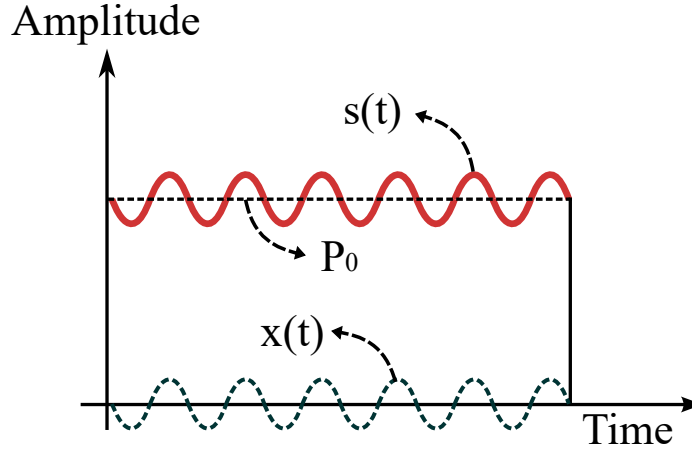
Figure 2.9: Transmitter Signaling Design

We define α as

$$\alpha \triangleq \frac{A}{P_0}. \tag{2.3.3}$$

Note that the value of α must be of order 10^{-1} in order to operate the transmit LEDs in its linear region, to minimise the flicker in illumination and to conform to the eye-safety standards of indoor illumination [6]. At the solar cell receiver, the received optical power creates a DC current I as indicated in Fig. 4.2, with an AC component of amplitude αI that carries the information while the DC component, I, is utilised for energy harvesting. As explained in Sec. 4.1, the AC and DC components of the transmitted signal will be separated using a bias tee circuit at the receiver.

2.3.2   Simulation Parameters

A single Silicon solar cell was simulated in this work. The characteristics of the solar cell considered are displayed in Table 2.2. Typical solid-state parameters of the solar cell we taken from [74, Chapter 7], as shown in Table 2.3. Unless otherwise cited, the

Parameter	Symbol	Value
Solar Cell Area	A_{cell}	100 cm^2
Short-Circuit Current	I_{sc}	3.8 A
Open-Circuit Voltage	V_{oc}	0.61 V
Fill Factor	FF	81%
Efficiency	η	18.7%

Table 2.2: Key characteristics of the simulated solar cell.

Parameter	Symbol	Value
Ideality Factor	η_{cell}	1
Doping Concentration (N-Type)	N_d	1×10^{19}
Doping Concentration (P-Type)	N_a	1×10^{16}
Bulk Semiconductor Size	L	300 μm

Table 2.3: Key characteristics of the simulated solar cell.

plots provided in this thesis are generated using MATLAB simulations [75].

For the simulations of this thesis, without the loss of generality, we assume a perfect LOS channel gain, i.e., $H(0) = 1$. The power spectral density of the noise in the solar cell receiver was studied in [52], and for our simulations, we have $N_0 = 1.646 \times 10^{-20}$. In order to stay within the linear region of the LED characteristics, α is set to $\alpha = 0.1$.

2.4   Conclusions

In this chapter, different components of the VLC system were studied. The differences between RF communication and VLC were highlighted. The IM-DD channel was introduced, and photodiodes were studied as semiconductor devices that enable

direct-detection. The importance of the responsivity and its dependence on the incident wavelength was investigated, which included the performance characteristics parameters of commonly used PDs along with a simple comparison between the different models.

In this chapter, the non-linear behaviour of LEDs in terms of their I-V and P_{opt}-I characteristics were analysed. Moreover, it was shown that the relative spectral output power of LED shifts and scales with a change in the temperature of the device. The optical wireless communications channel was modelled as a bandpass LTI system with AWGN. The LOS and NLOS links were illustrated, and the DC channel gains for the communication links were derived.

Finally, the SLIPT system model investigated in this thesis was delivered, and the simulation parameters used were displayed. In the next chapter, the DC characteristics of the solar cell are going to be covered, and simulations results of the solar cell will be displayed.

Chapter 3

Solar Cell Characteristics

In this chapter, we present an overview of the physics of solar cells, their operating point and characteristic-defining parameters. A DC model for the solar cell is derived from fundamental principles. The DC model is then simulated on MATLAB from which I-V and P-V curves are plotted to demonstrate the dependency of the solar cell to irradiance. In this chapter, we show that the power harvested from the solar cell is maximum at a specific operating voltage. In order to quantify solar cells' data reception capabilities, the small-signal parameters of the cell have to be derived to construct a small-signal (AC) equivalent model, from which the bandwidth is calculated. In this chapter, the AC model of the solar cell is introduced, and the simulation results of the AC model, are illustrated.
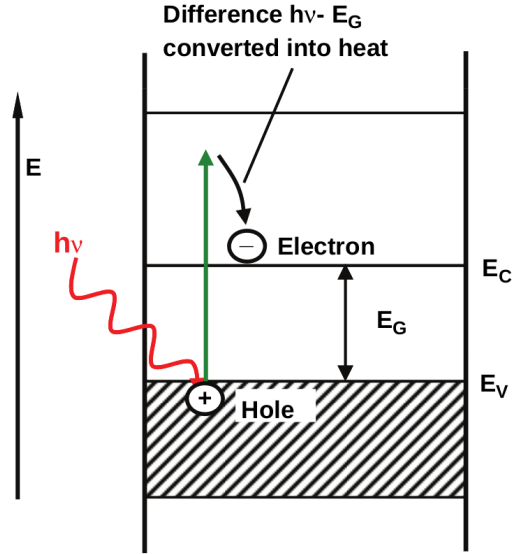
Figure 3.1: The photovoltaic effect: a photon with energy $h\nu \geq E_g$ excites an electron to the conduction band, leaving a hole in the valence band [76].

3.1   The Photovoltaic Effect

The photovoltaic effect is the process of generating electrical current from material that is under light radiation and is the underlying phenomenon that explains photocurrent generation in solar cells [74]. The electron-hole generation is shown in Fig 3.1. The energy E carried by a single photon is given by the Einstein-Plank relation

$$E = h\nu, \tag{3.1.1}$$

where h is the Plank constant, and ν is the electromagnetic frequency of the photon. When light is radiated on the surface of the solar cell, the photon with sufficient energy $h\nu > E_g$, where E_g is the band gap of the semiconductor, can excite an electron from the valence band into the conduction band, leaving a hole in the valence band [76].

The built-in electrical field within a photovoltaic device or a solar cell pn junction

immediately separates the photogenerated electron-hole pair. With the electrons and holes drifting into p side and the n side, respectively, an external photocurrent is generated that flows through an external load [70]. In the next section, the DC equivalent circuit for the solar cell is going to be developed.

3.2   Solar Cell DC Equivalent Circuit

The electrical equivalent circuit for an ideal photovoltaic cell is shown in Fig 3.2. The incidence of light on the solar cell creates a proportional photogenerated current, I_{ph}. When there is no load at the cell terminals, i.e. $R_L = 0$, I_{ph} is the short-circuit current. In open-circuit conditions, we have $I_{ph} = I_{sc}$ and no output current. When $R_L \neq 0$, a potential difference, V is built at the cell terminals, which forward biases the diode, which generates a current I_D according to the ideal diode equation,

$$I_D = I_0 \left(e^{\frac{V}{V_T}} - 1 \right), \tag{3.2.1}$$

where I_0 is the reverse saturation current, V_T is the thermal voltage given by

$$V_T = \frac{kT}{q}, \tag{3.2.2}$$

where k is the Boltzmann constant, T is the Temperature in Kelvin and q is the charge of an electron. Here, a portion of I_{ph} goes through the diode; hence, the output current I is less than the short-circuit current. As the value of R_L increases, V also increases which causes I_D to become larger. Thus, the I-V characteristics of the ideal
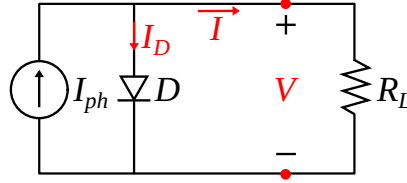
Figure 3.2: DC equivalent circuit for ideal solar cell
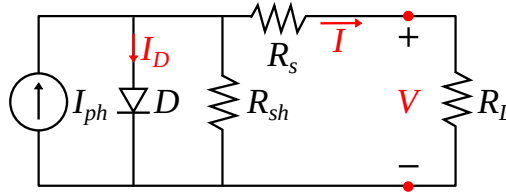
Figure 3.3: DC equivalent circuit of solar cell

solar cell is given by [74]

$$I(V) = I_{ph} - I_D = I_{ph} - I_0 \left(e^{\frac{V}{V_T}} - 1 \right). \tag{3.2.3}$$

Though the above model simplifies the system analysis, it is not very realistic. A more realistic equivalent circuit for a solar cell can be obtained by including a series resistance R_s to model the material and contact resistance, and a resistance R_{sh} in parallel with the diode to model the leakage current [74]. This equivalent circuit is shown in Fig. 3.3 and the I-V characteristic of this circuit is given by

$$I(V) = I_{ph} - I_0 \left(e^{\left(\frac{V + I R_S}{\eta_{\text{cell}} V_T} \right)} - 1 \right) - \frac{V + I R_s}{R_{sh}}, \tag{3.2.4}$$

where η_{cell} is the ideality factor and typically lies within the range $\eta_{\text{cell}} \in [1, 2]$ [74]. Note that the characteristic equation does not directly describe the current I in terms of the cell voltage V for $R_S \neq 0$. The voltage can be expressed as a direct function

of I for $R_{sh} = \infty$ as

$$V = \eta_{\text{cell}} V_T \ln \left(\frac{I_{ph} - I}{I_0} + 1 \right) - I R_S. \tag{3.2.5}$$

Assuming that R_s is very small and R_{sh} is of the order of several kΩ, the DC output power is derived from (3.2.5) and (3.2.4) as

$$P(V) = I \times V = V \left(I_{ph} - I_0 \left(e^{\frac{V}{\eta_{\text{cell}} V_T}} - 1 \right) \right). \tag{3.2.6}$$

3.2.1   Current-Voltage Characteristics

The operating voltage or the operating point of the solar cell is its output voltage, V. The I-V characteristic of a solar cell, as stated in (3.2.4), is plotted for several irradiance values in Fig. 3.4. It is clearly apparent that the output current is constant for the majority of the voltage range; for this reason, solar cells are modelled as a current source in contrast to batteries that are modelled as voltage sources. In constant, it can be seen that the I-V curves scale vertically with irradiance since the I_{ph} is directly proportional to the irradiance. Note that the voltage at which the plot crosses the x-axis, is V_{oc}. The value of V_{oc} scales logarithmically with respect to I_{ph} and hence, the irradiance level. The open-circuit voltage V_{oc} can be approximated by substituting $I = 0$ in (3.2.5) to get

$$V_{OC} \approx \eta_{\text{cell}} V_T \ln \left(\frac{I_{ph}}{I_0} + 1 \right). \tag{3.2.7}$$

Given that $I_{sc} \approx I_{ph}$, an approximation for I_o can be derived from (3.2.7) by
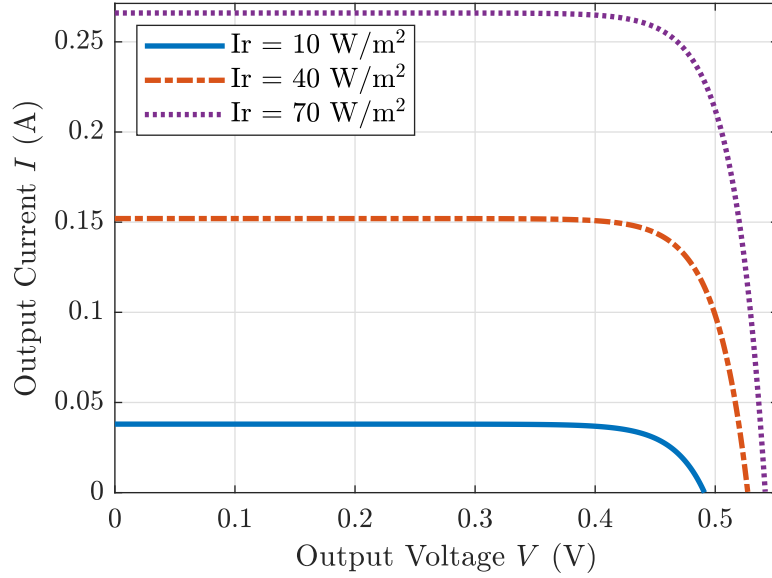
Figure 3.4: Solar Cell Curves

substituting $I_{sc} = I_{ph}$ to get

$$I_0 \approx \frac{I_{sc}}{e^{\left(\frac{V_{oc}}{\eta_{\text{cell}} V_T} - 1\right)}}. \tag{3.2.8}$$

It is possible to express the current I in terms of the voltage V using the Lambert W function

$$I(V) = \frac{R_{sh}(I_0 + I_{ph}) - V}{R_s + R_{sh}} - \frac{\eta_{\text{cell}} V_T}{R_s} W \left\{ \frac{R_s I_0 R_{sh}}{\eta_{\text{cell}} V_T (R_s + R_{sh})} \exp\left(\frac{R_{sh}(R_s I_{ph} + R_s I_0 + V)}{\eta_{\text{cell}} V_T (R_s + R_{sh})}\right) \right\}, \tag{3.2.9}$$

where $W(x)$ is the solution of y in $ye^y = x$ for any complex number x. Other parameters of the solar cell could also be expressed in the direct form using the Lambert W function. [77].

42
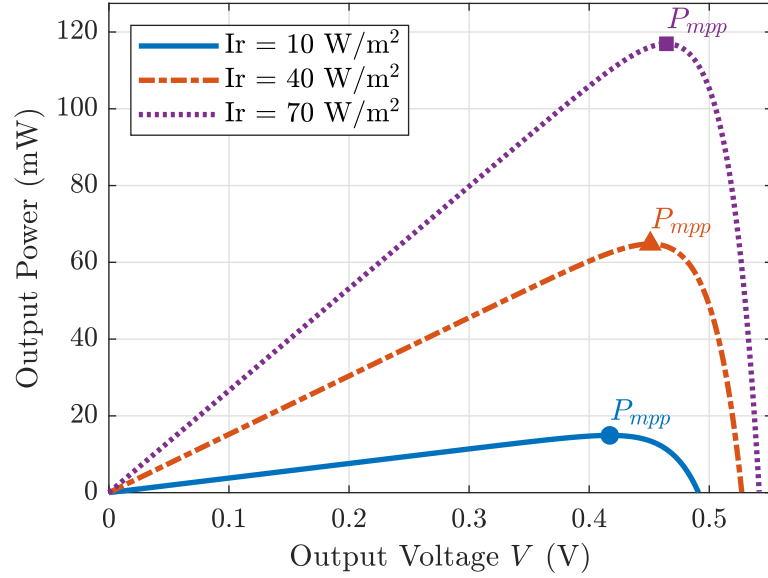
Figure 3.5: *P-V* characteristics of solar cell

3.2.2   Power-Voltage Characteristics

The *P-V* characteristics of the simulated solar cell is a plot of the solar cell's output power P and DC voltage V, given by (3.2.6). In Fig 3.5 the P-V characteristics of the simulated solar cell is plotted for different irradiance levels. Note that the solar cell operates within the voltage range $V \in (0, V_{oc}]$. It would not be possible to produce energy outside the aforementioned range. Depending on the DC terminal conditions, the output power from the solar cell will vary. The maximum power point (P_{mpp}) is defined as the maximum output power of a given solar cell. As it is shown in Fig 3.5, each *P-V* curve has a global maximum denoted by P_{mpp}. The voltage and output current corresponding to P_{mpp} are defined as V_{mpp} and I_{mpp}, respectively, such that

$$P_{mpp} = I_{mpp} \times V_{mpp}. \tag{3.2.10}$$

As expected, the value of P_{mpp} scales proportionally with respect to the irradiance. It is interesting to note that in order to reach the maximum power, the output current decreases due to an increase in I_D in (3.2.3). As the value of V exceeds V_{mpp}, the output power starts to decrease. In order to ensure maximum power transfer takes place from the solar cell under different irradiance values, maximum peak power tracking algorithms are created to track the P_{mpp} point [78]. Sec. 3.4 presents this approach in more detail. In the next section, other important characteristics parameters associated with solar cells will be introduced.

3.3   Key Solar Cell Characteristics

Solar cells are fabricated in various sizes using different materials such as crystalline silicon cells, multijunction gallium arsenide (GaAs) cells and thin-film solar cells [79, 80]. In order to define efficiency in solar cells, all parameter readings must be done under standard testing conditions (STC). The STC for solar cells is defined as a temperature of 25 °C, an irradiance of 1000 W/m^2 and the Air Mass 1.5 Spectrum. In this section, the key characteristics of solar cells are explained.

3.3.1   Fill Factor

$$FF = \frac{I_{mpp}V_{mpp}}{I_{sc}V_{oc}}. \tag{3.3.1}$$

By inspecting Fig. 3.6, it can be observed that the V_{mpp} and I_{mpp} values are smaller than V_{oc} and I_{sc}, respectively. This gap exists due to the internal losses that occur within the solar cell pn junction. The fill factor (FF) is a metric that quantifies this
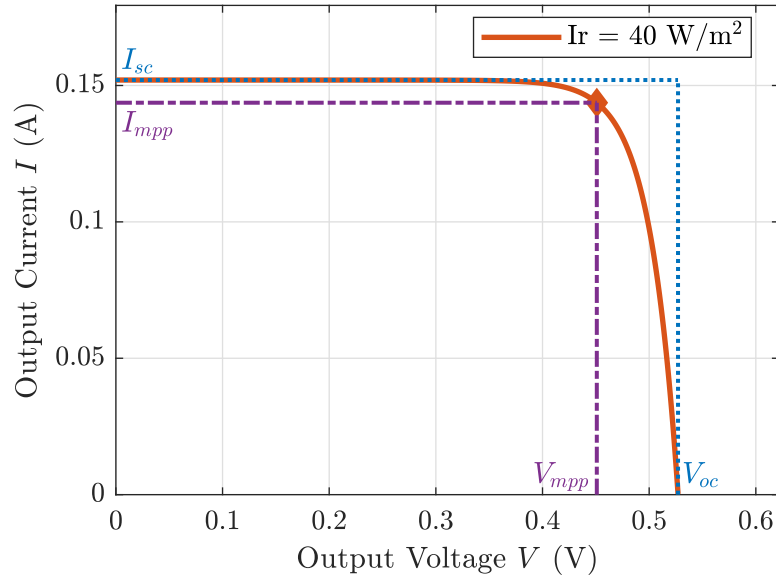
Figure 3.6: *I-V* curve for a single irradiance.

gap and is used to describe solar cell efficiency, defined as the ratio of the area of the rectangle indicated by the purple boarders to the area of the blue rectangle, expressed as

In a sense, the fill factor describes the '*squareness*' of the *I-V* characteristics of the solar cell. In the VLC literature, the FF value is used along with I_{sc} and V_{oc} to describe the output power of the solar cell receiver as

$$P = FF \times I_{sc}V_{oc}. \tag{3.3.2}$$

Cell Type	Area (cm^2)	J_{sc} (mA/cm^2)	V_{oc} (V)	FF	Efficiency (%)
Si crystalline	79.0	42.65	0.738	84.9	26.7 ± 0.5
Si multicrystalline	3.923	41.08	0.674	80.5	22.3 ± 0.4
Si amorphous	1.001	16.36	0.896	69.8	10.2 ± 0.3
GaAs thin film	0.998	29.78	1.127	86.7	29.1 ± 0.6
GaAs multicrystalline	4.011	23.2	0.994	79.7	18.4 ± 0.5
InP crystalline	1.008	31.15	0.939	82.6	24.2 ± 0.5

Table 3.1: Key performance characteristics for different types of solar cells [81]

3.3.2 Efficiency

The efficiency of the solar cell, η, is defined as the ratio between P_{in} and the input power irradiated onto the solar cell:

$$\eta = \frac{I_{mpp}V_{mpp}}{P_{in}} = \frac{I_{sc}V_{oc}FF}{P_{in}}. \tag{3.3.3}$$

The expression for η is better described in terms of J_{sc}, the short-circuit current per unit area of the solar cell and Ir, the incident irradiance:

$$\eta = \frac{J_{sc}V_{oc}FF}{Ir} \tag{3.3.4}$$

Using J_{sc} to describe the short circuit current density at Ir = 1000 W/m^2 allows for comparison between solar cells of different physical dimensions. The highest confirmed solar cell efficiency values for some cell types along with their characteristic parameter values are displayed in Table 3.1. Note that the materials with higher short-circuit current density J_{SC} have a smaller open-circuit voltage V_{OC}.
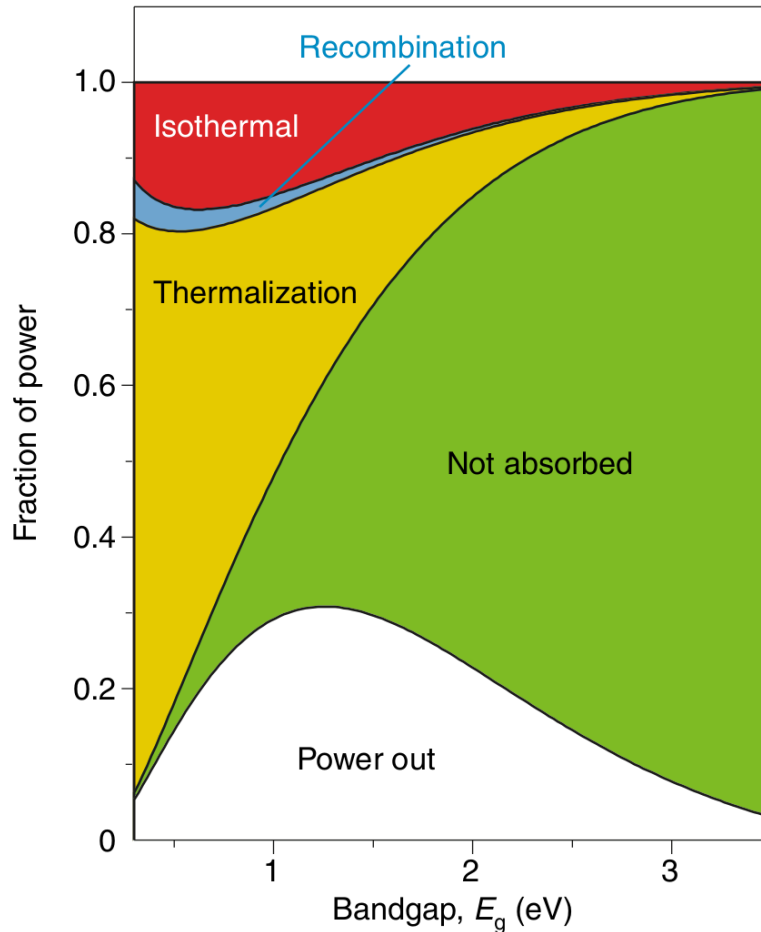
Figure 3.7: The power losses of a solar cell under standard testing conditions, normalised with respect to an irradiance of 1000 W/m² [82]

3.3.3 Theoretical Limits on Efficiency

For single-junction solar cells, there is a theoretical efficiency quantified by William Shockley and Hans-Joachim Queisser in 1961 [84]. Fig. 3.7 demonstrates the processes through which the power loss occurs under the assumptions made in [84]. From Fig. 3.7, it can be observed that as the band gap of the semiconductor increases, the fraction of absorbed photons decreases. When the incident photon energy exceeds

Figure 3.8: Plot of the theoretical Shockley-Queisser efficiency limit (solid black line) as a function of the semiconductor's band gap E_g. The grey lines indicate 75% and 50% of the limit, respectively [83].

that of the band gap, the excess energy is lost as heat; this is referred to as the thermalisation loss. As the band gap decreases, the thermalisation loss becomes the determining factor for the efficiency of th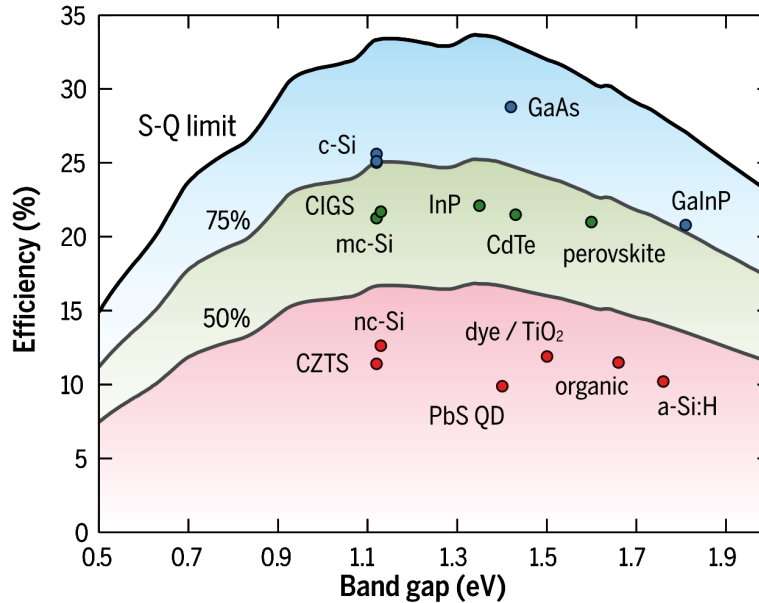e cell. The isothermal loss indicated in red represents the loss of power in the process of separation and collection of the electrons and holes. The recombination loss, indicated in blue, accounts for when the electron-hole pair created from the incident photon is not separated and eventually recombine to radiate a photon. Fig. 3.8 displays the theoretical Shockley-Queisser limit on the efficiency of solar cells in terms of the band gap E_g of the semiconductor material. It is important to note that the Shockley-Queisser limit is calculated under the assumption that the maximum power is delivered to an external load connected to the terminals of the solar cell. The highest recorded efficiency values for solar

cells of different material are also included in Fig. 3.8. Note that the majority of the recorded efficiency values are below 75% of the theoretical limit shown.

One way to surpass the Shockley-Queisser limit is to try and absorb photons of a higher range of frequencies; this is realised through Tandem solar cells [85]. Multi-junction (Tandem) solar cells consist of n pn junctions of different semiconductor material where $n > 1$. Hence, each pn junction has a different band gap energy E_g and therefore absorb photons of different frequencies. In effect, a different part of the spectrum is absorbed by each pn junction. By relaxing the assumptions made in the derivation of the Shockley-Queisser limit, the upper limit of the theoretical efficiency of the multi-junction solar cells is proved to reach 42% at $n = 2$ and 53% at $n = 4$ under an irradiance of 1000 W/m². By letting $n \to \infty$, which implies an infinite number of junctions in with $E_g \in (0, \infty)$, a theoretical efficiency of 86.8% was calculated for an irradiance of 45.0 MW/m² [85, 86].

3.4   Maximum Peak Power Tracking

The theoretical limits on the efficiency of solar cells are calculated under the assumption that the maximum power is delivered from the cell to an external load which is also described as the maximum power point (MPP). As it is apparent from Fig. 3.5, the global maximum of each irradiance level corresponds to a unique operating point, V_{mpp}. Given that the MPP point is also dependant on the temperature, solar power production is highly dependant on weather conditions as it affects both the temperature and the amount of incident irradiance [87]. When operating to produce power, it is important to make sure that the solar cell operates close to the $V = V_{mpp}$ point despite the stochastic nature of the irradiance and ambient temperature [88].
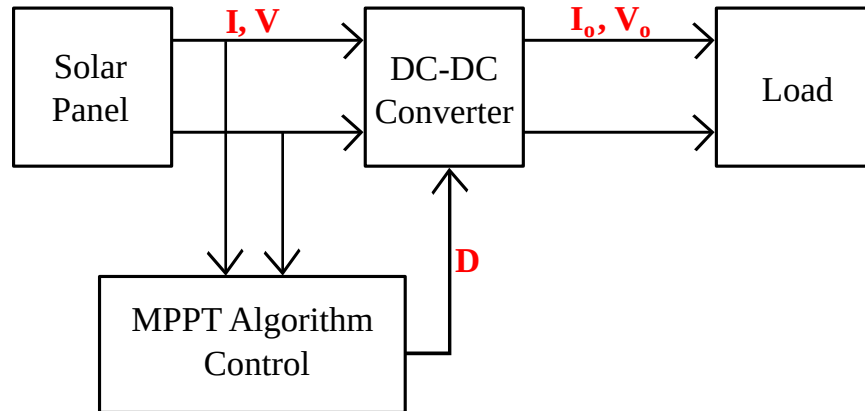
Figure 3.9: Maximum peak power tracking.

Maximum peak power tracking (MPPT) algorithms adjust the DC terminal characteristics of the solar cell so that the maximum power is extracted. Several MPPT algorithms have been developed to optimise the performance of photovoltaic devices by controlling the duty cycle, D, of the DC-DC converters to control the operating point of the solar cells [78].

The perturb and observe (P&O) algorithm, shown in Fig. 3.10 is a widely used MPPT algorithm due to its simplicity for implementation [89]. The P&O algorithm is based on the following principle: when the operating voltage of a given cell is perturbed, i.e. increased or decreased, and if the output power of the cell increases, this implies that the operating point has become closer to the MPP point. On the other hand, if the perturbation results in a decrease in output power, the direction of the perturbation must be switched. Note that DC-DC converters are employed to enable the last stage of the algorithm in which the operating voltage of the cell is either decreased or increased [89, 90].
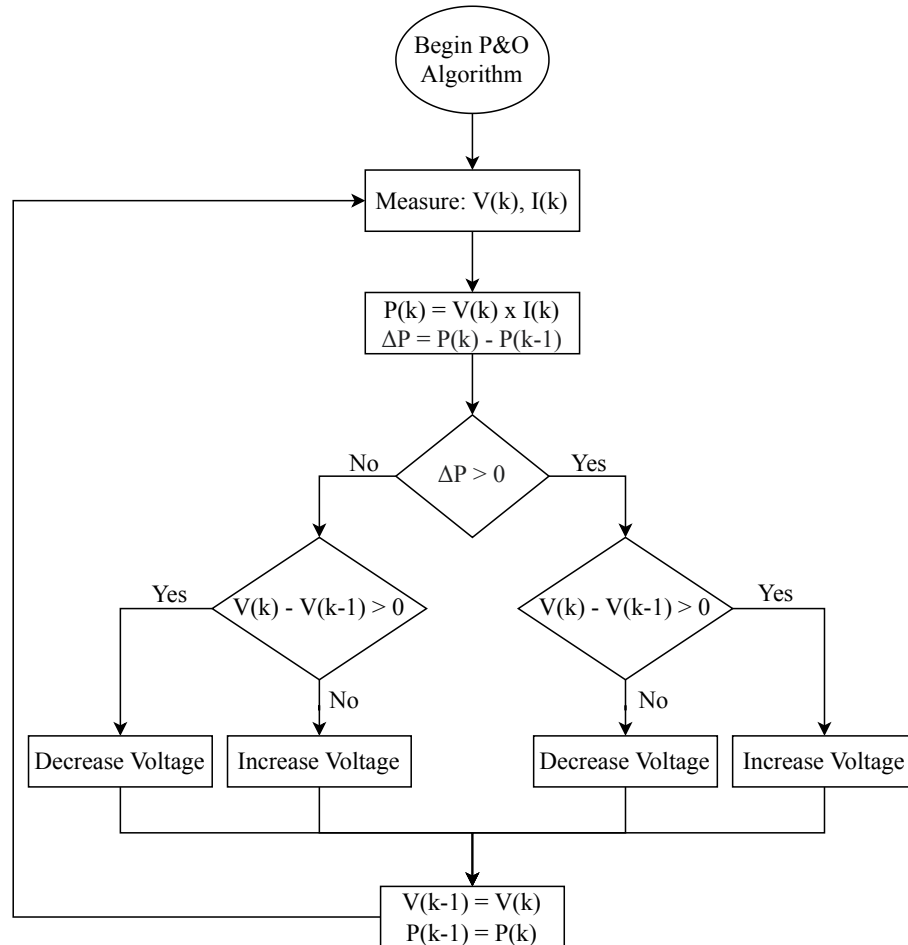
Figure 3.10: Flowchart diagram of the perturb and observe algorithm

3.5   AC Model of Solar Cell

While solar cells are built to produce and operate in DC mode, as described in Sec. 3.2, analysing their performance as optical intensity receivers require the development of an AC model for the cell. The AC behaviour of the solar cell was investigated, and an equivalent circuit was developed for the first time in [51, 91]. The small-signal equivalent circuit is shown in Fig. 3.11. Note that the series resistance R_s and the parallel resistance R_{sh} from the DC analysis presented in Sec. 3.2 are also present in
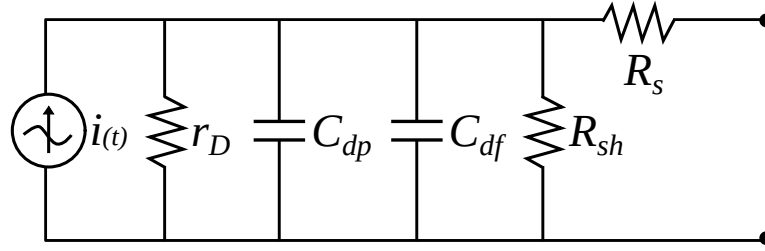
Figure 3.11: Small-signal (AC) equivalent of the solar cell.

the AC equivalent model. In addition, r_d represents the dynamic (i.e., small-signal) resistance of the pn junction and is expressed as [91]

$$r_d = \frac{\eta KT}{qI_0} e^{\frac{-V}{\eta_{\text{cell}} V_T}}. \tag{3.5.1}$$

By studying the pn junction of the solar cell under the forward bias operation, an expression for the cell's total voltage-dependent capacitance is developed in the following sections.

3.6   Solar Cell pn Junction

An intrinsic semiconductor consists of an ideal crystal structure with no impurities. A pn junction consists of a piece of extrinsic semiconductor which is p-type doped on one side and n-type doped on the other side. Fig. (3.12) shows a pn junction under equilibrium [92]. On the P-side we have an excess of holes, and on the N-side, we have an excess of electrons due to the acceptors and donor dopant atoms, respectively. This induces a concentration gradient that results in holes in the P-side to diffuse down the concentration gradient, into the N region. Similarly, electrons in the N-side diffuse down the concentration gradient, into the P region. Once these electrons and holes
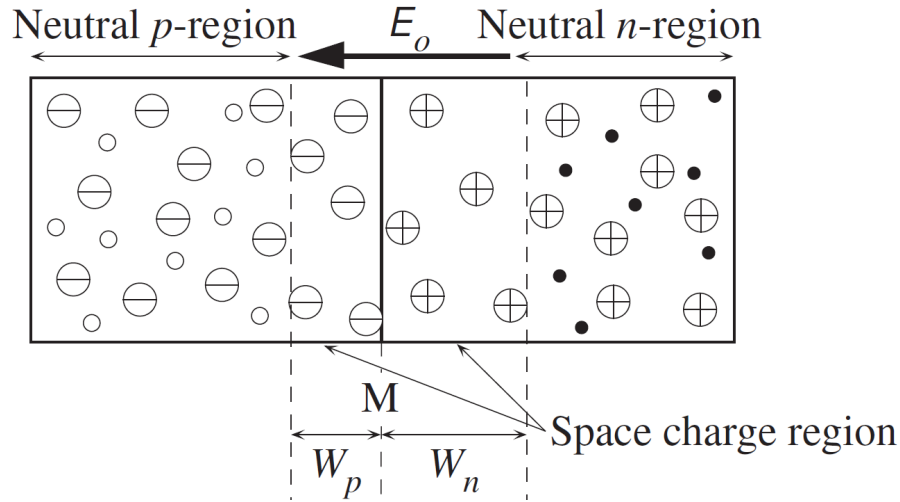
Figure 3.12: The pn junction. [92]

have just diffused into the other side, they will recombine with holes and electrons. This results in a junction depleted of carriers and only consists of positively charged donor ions and negatively charged acceptor ions. This is the depletion region or the space charge region, as shown in Fig. 3.12.

As it is apparent, an electric field E_0, is formed in the direction of positively charged ions to the negatively charged ions. This field applies a force to the free carriers in the opposing direction to carrier diffusion due to the concentration gradient. As more electrons and holes diffuse into the left and right side of the junction, respectively, more static charge is left behind in the depletion region, causing a stronger internal filed E_0. This procedure will take place until the number of carriers diffusing down the concentration gradient is balanced by the number of carriers drifting due to E_0. This is the equilibrium state. This internal electric field, E_0, corresponds to a built-in potential V_0 across the junction. The following expressions could be used to

calculate V_0

$$V_0 = \frac{qN_aN_dW_0^2}{2\varepsilon(N_a + N_d)}, \tag{3.6.1}$$

$$W_0 = W_n + W_p, \tag{3.6.2}$$

$$V_0 = \frac{kT}{q} \ln\left(\frac{N_aN_d}{n_i^2}\right), \tag{3.6.3}$$

Where n_i^2 is the intrinsic concentration, N_a is the acceptor atom concentration, N_d is the donor atom concentration, $\varepsilon = \varepsilon_0\varepsilon_r$ is the absolute permeability and W is the width of the depletion region. Note that on the last equation, the built-in voltage is expressed in terms of N_d , N_a and n_i^2 which are known semiconductor parameters. By rearranging the first equation, W_0 is expressed in terms of V_0

$$W_0 = \left[\frac{2\varepsilon(N_a + N_d)V_0}{qN_aN_d}\right]^{1/2}. \tag{3.6.4}$$

Observe that the width of the junction is proportional to the potential difference across the junction; this is an important result as we will see later, one component of the capacitance of the junction is inversely proportional to the width of the depletion region, and it is this capacitance that determines our bandwidth for data reception.

3.7   Solar Cell Capacitance

The capacitance of the solar cell is of great importance, as it determines the bandwidth of our receiver, as derived in Sec. 4.1.2. The two capacitances in parallel, C_{df} and

C_{dp}, represent the diffusion capacitance and depletion capacitance associated with the pn junction of the solar cell, respectively. Depletion capacitance occurs both in the forward and bias operating modes and diffusion capacitance which only arises in the forward bias conditions.

3.7.1   Depletion Capacitance

The depletion capacitance (C_{dp}) exists because of positive and negative charges in the depletion region of the junction separated by a distance w which depends on the DC operating voltage, V. The value of C_{dp} can be approximated as [92]

$$C_{dp}(V) = \frac{\varepsilon A_{cell}}{w} = A_{cell}\left[\frac{2(N_a + N_d)(V_0 - V)}{\varepsilon q N_a N_d}\right]^{-\frac{1}{2}},\qquad (3.7.1)$$

where N_a is the acceptor atom concentration, N_d is the donor atom concentration and V_0 is the built-in voltage of pn junction.

3.7.2   Diffusion Capacitance

The diffusion capacitance arises due to the accumulation of excess minorities charge carriers in the pn junction [70, 91]. The expression for the diffusion capacitance, also named the chemical capacitance [93], is expressed as [94]

$$C_{df}(V) = \frac{A_{cell} q L n_0}{V_T} e^{\frac{V}{V_T}},\qquad (3.7.2)$$

where n_0 is the minority carrier density in equilibrium and L is the bulk semiconductor size.
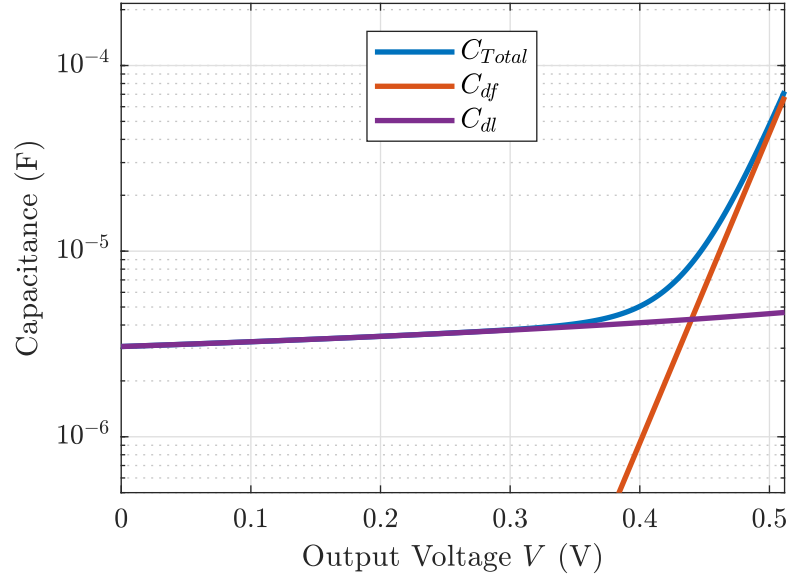
Figure 3.13: Capacitance of Solar Cell as a function of operating point, V.

Since C_{df} and C_{dp} are in parallel, the total capacitance of the receiver circuit is expressed as

$$C_T(V) = C_{df}(V) + C_{dp}(V). \tag{3.7.3}$$

Fig. 3.13 shows the plot of $C_T(V)$ along with $C_{df}(V)$ and $C_{dp}(V)$ as a function of V. Note that for $V < 0.35$ V, the total capacitance is approximately equal to the depletion capacitance while the contribution of the diffusion capacitance dominates the total capacitance at higher bias voltages.

3.7.3   Comparison of Solar Cells and Photodiodes

It is important to realise that in contrast to the photodiodes that operate in the reverse bias region, solar cells operate in the forward bias region. Hence, solar cells exhibit greater capacitance due to the contributions of $C_{df}(V)$, which only occurs in

forward bias, which directly limits the bandwidth of the solar cell-based receiver. On the other hand, photodiodes offer a much larger bandwidth and are more suitable to detect optical signals while incapable of producing power.

In Chapter 2, photodiodes were introduced as semiconductor devices that enabled the IM-DD channel to be realised. While photodiodes have been used to detect high-speed optical intensity signals for the past decades, they require power to operate [70]. In contrast, solar cells have the capability to produce power while functioning as optical receivers [71]. While both devices ordinarily consist of a pn junction, the operation of a solar cell is fundamentally different from photodiodes; in solar cells, the pn junction operates under forward bias. Whereas, in the case of a photodiode, the pn junction operates under reverse bias.

3.8   Conclusions

In this chapter, an overview of the fundamental concepts of solar cell operation, application and efficiency were presented. The effect of irradiance on the solar cell's output current, voltage and power was demonstrated through MATLAB simulations. The fundamental parameters that define the solar cell's characteristics, J_{sc}, V_{oc}, η and FF were introduced. It was shown that the cell's power reaches the global maximum at the $V = V_{mpp}$ operating point. It was shown how the perturb and observe MPPT algorithm identifies and reaches maximum power point by controlling the duty cycle of a DC-DC converter. In the previous studies that used solar cells as VLC receivers, the DC terminal characteristics of the solar cells were optimised solely to maximise the power received.

In this chapter, the small-signal equivalent circuit of the solar cell was presented.

The total capacitance, $C_T(V)$ of the solar cell was derived as a function of the operating voltage of the cell, V. It was shown that the diffusion capacitance grows exponentially with V, and eventually dominates $C_T(V)$ at higher values of V.

Chapter 4

Adaptive Solar Cell-based Receiver Design

In this chapter, a novel proposed adaptive-SLIPT receiver is presented and analysed. While previous approaches to SLIPT assume a constant, known bandwidth for the solar cell receiver, in this design, it is shown that the bandwidth of the solar cell is not constant and is a function of the solar cell's DC operating voltage. The DC analysis of the solar cell was reviewed in Sec. 3.2, where it was illustrated that the output power of the solar is a function of its DC operating voltage. Later in Sec. 3.4 it was shown that this operating voltage could be controlled using DC-DC converters, enabling MPPT algorithms to draw the maximum power from a given solar cell. The small-signal (AC) equivalent model of the solar cell was presented in Sec. 3.5. It was shown that the solar cell has two main capacitances, $C_{df}(V)$ and $C_{dp}(V)$, are voltage dependant.

The designed SLIPT receiver uses DC-DC converters to control the operating voltage of the solar cell, which directly defines the solar cell capacitance and output

power. By deriving the expression for the bandwidth of the proposed receiver, it is shown through MATLAB simulation that the bandwidth is also dependant on the DC operating voltage of the cell.

4.1   Adaptive Solar Cell Based SLIPT Receiver

The block diagram of the proposed adaptive-SLIPT receiver is shown in Fig. 4.2. As mentioned in Sec. 2.3.2, the channel impulse response is assumed to be ideal with a DC gain of $H(0) = 1$. In the adaptive-SLIPT receiver, the solar cell collects the optical signal and converts it to an equivalent electrical current. A bias tee circuit is then used to split the current into DC and AC components. The DC component is used for power harvesting, i.e., connected to a load while the AC component is fed to a transimpedance amplifier (TIA) and then fed into modules that perform demodulation and decoding. Notice that the boost converter determines the DC operating voltage, V, for the solar cell in order to adapt the trade-off between rate and power collection. In the previous designs, the boost converter was not used as the DC operating point was constant.

4.1.1   DC Analysis

The power harvested from the solar cell, i.e., $P = IV$, varies with the operating voltage V. From (3.2.4), the value of the operating voltage that leads to maximum power harvesting, i.e., $V = V_{mpp}$, can be computed. By placing a DC-DC converter [95] between the cell's output terminals and the load resistance, and changing the duty cycle of the DC-DC converter's switch, the operating DC voltage V at the cell's
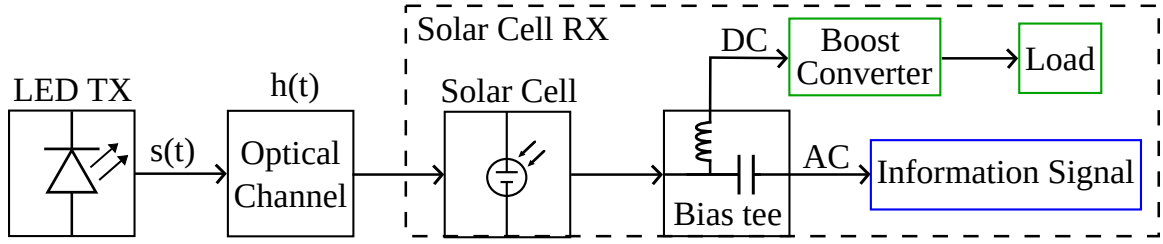
Figure 4.1: Adaptive-SLIPT receiver design.
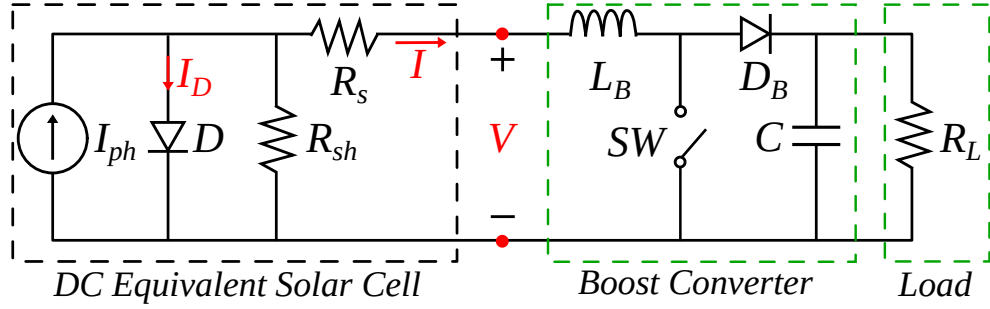
Figure 4.2: DC Equivalent Circuit

terminals can be set to the desired value [96].

4.1.2   Receiver Bandwidth

The AC equivalent circuit of the Adaptive-SLIPT solar cell-based receiver is shown in Fig. 4.3. Note that R_c is the internal resistance of the transimpedance amplifier (TIA), which can be assumed to be small and negligible.

Note that due to the decoupling capacitance in Fig. 4.1, the signal through R_c has no DC component. The bandwidth, $B(V)$, of the solar cell-based receiver can be computed as

$$B(V) = \frac{1}{2\pi R_T(V)C_T(V)}, \tag{4.1.1}$$
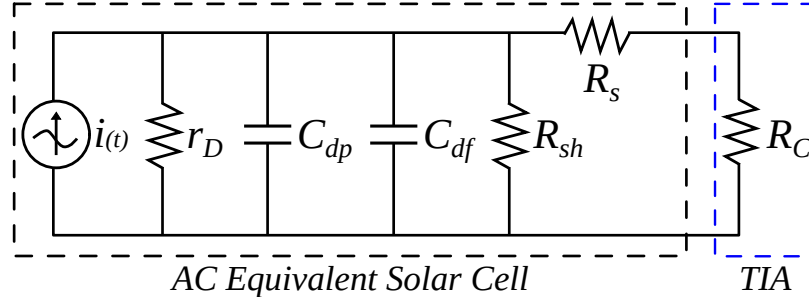
Figure 4.3: Small-signal (AC) equivalent of the Adaptive-SLIPT solar cell-based receiver.

$$R_T = R_{sh} \parallel (R_s + R_c) \parallel r_d. \tag{4.1.2}$$

Note that the bandwidth is a function of R_T and C_T, which in turn are functions of the DC operating voltage of the solar cell, V. Fig. 4.4 shows plots of the receiver bandwidth as a function of the operation voltage, V. The bandwidth (4.1.1) decreases with increasing V, as shown in Fig. 4.4. Notice, however, that the bandwidth is not directly affected by the irradiance level as the solar cell capacitance is not a function of input irradiance [94].

Therefore, *the electrical bandwidth and thereby, the supported data rate, of the solar cell-based optical receiver depend on V*. Thus, one has to choose the operating voltage to simultaneously maximise the harvested power while guaranteeing a given supported data rate in a solar cell-based optical receiver.

In the next chapter, a closed-form expression for the supported rate of the solar cell-based receiver is derived and the trade-off between its supported rate and harvested power quantified.
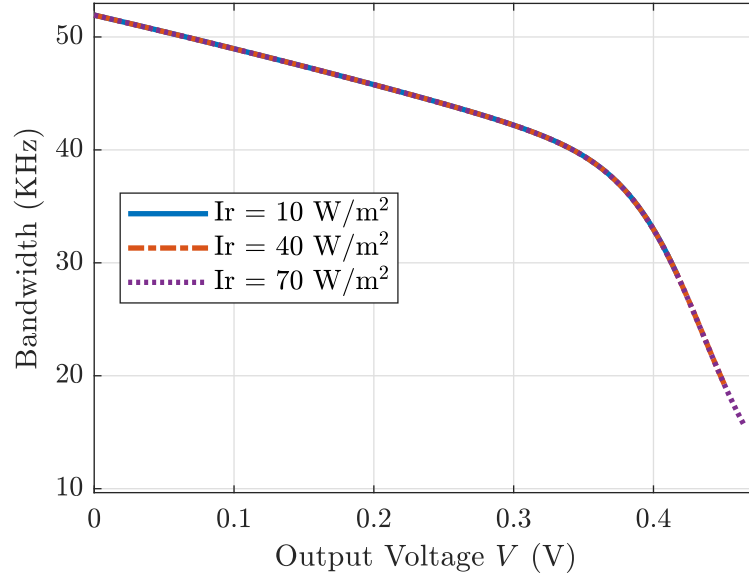
Figure 4.4: Bandwidth as a function of the operation voltage,V

4.2   Conclusions

In this chapter, the adaptive-SLIPT receiver was introduced. By employing a boost DC-DC converter, the receiver is able to control the solar cell's operating voltage V.

In addition, the expression for $C_T(V)$ was used to derive the bandwidth of the receiver. The bandwidth was shown to be dependant on V, where the capacitors had the highest contribution in the bandwidth of the adaptive-SLIPT receiver. In the previous literature, the electrical bandwidth of the solar cell was assumed to be constant; however, using our expression for $B(V)$, it is clearly apparent that a solar cell-based receiver with a pn junction architecture has a voltage-dependent bandwidth.

Finally, it was shown that the voltage-dependent $C_T(V)$ is significant and determines the bandwidth of the receiver, which, in turn, determines the supported data rate.

Chapter 5

Rate-Power Trade-off

In the previous chapter, a voltage-dependent expression for the bandwidth of the proposed receiver was derived. In this chapter, a lower bound for the Shannon capacity (supported data rate) is derived for the signalling scheme proposed in (2.3.1). Using the expression for the supported data rate R, and the equation for solar cell power, P, solar cell power equation (3.2.6), a trade-off between P and R is quantified for the first time and presented through MATLAB simulation results for different irradiance levels.

Finally, a system design problem is formulated as an optimisation to find the optimum solar cell DC operating voltage to obtain a trade-off between rate and power for a given battery charge state and background irradiance.

5.1   Lower bound on Channel Capacity

The received signal Y corresponding to $y(t)$ from Sec. 2.2 at the receiver is given by

$$Y = X + N, \tag{5.1.1}$$

where X is the transmitted signal corresponding to $x(t)$ in (2.3.1) and N is the zero-mean additive Gaussian noise with variance σ corresponding to $n(t)$ from Sec. 2.2. The noise variance is given by

$$\sigma^2 = B(V)N_0, \tag{5.1.2}$$

where N_0 is the thermal noise power per unit bandwidth. Considering the signalling shown in (2.9), we find that the AC component of the transmitted signal is bounded by a peak-to-peak amplitude A, such that

$$X \in \left[\frac{-A}{2}, \frac{+A}{2} \right], \tag{5.1.3}$$

$$\mathbb{E}\{X\} = 0. \tag{5.1.4}$$

Shannon's channel capacity, C, is defined as [61]

$$C = \sup_{f_X(x) \in \mathcal{F}} I(X;Y), \tag{5.1.5}$$

where $I(X;Y)$ is the mutual information between X and Y, $f_X(x)$ is the probability density of X and $\mathcal{F}$ is the set of distributions of X that satisfy the constraints in

(5.1.3) and (5.1.4).

In order to find a lower bound for the channel presented, any distribution $f_X(x)$ such that $f_X(x) \in \mathcal{F}$ can be used to calculate $I(X;Y)$. While this procedure would indeed result in a lower bound, it may not be close to the actual capacity. The aim is to find a tight lower bound that is close to the capacity. The entropy-power inequality enables us to achieve a tight lower bound: for two independent X_1 and X_2 density distributions, we have [97]:

$$2^{2h(X_1+X_2)} \geq 2^{2h(X_1)} + 2^{2h(X_2)}. \tag{5.1.6}$$

The inequality in (5.1.6) becomes an equality when X_1 and X_2 are Gaussian distributions. The lower bound for the channel capacity, C is derived as follows [97]:

$$C \geq I(X;Y) = h(Y) - h(Y|X), \tag{5.1.7}$$

$$= h(X+N) - h(X+N|X), \tag{5.1.8}$$

$$= h(X+N) - h(N), \tag{5.1.9}$$

By applying the entropy-power inequality in (5.1.6), a lower bound for $h(X+N)$ is derived as

$$h(X+N) \geq \frac{1}{2}\log\left(2^{2h(X)} + 2^{2h(N)}\right), \tag{5.1.10}$$

hence, by substituting (5.1.10) into (5.1.9), the expression for the channel capacity

lower bound is as follows [98]:

$$C \geq I\left(X;Y\right) \geq \frac{1}{2}\log\left(2^{2h(X)} + 2^{2h(N)}\right) - h\left(N\right). \qquad (5.1.11)$$

Given that for $N \sim \mathcal{N}(0, \sigma^2)$. the differential entropy is computed as

$$h\left(N\right) = \frac{1}{2}\log\left(2\pi e\sigma^2\right), \qquad (5.1.12)$$

equation (5.1.10) simplifies to

$$C \geq I\left(X;Y\right) \geq \frac{1}{2}\log\left(1 + \frac{2^{2h(X)}}{2\pi e\sigma^2}\right). \qquad (5.1.13)$$

By selecting the maximum entropy probability distribution for X such that, $f_X^*(x) \in \mathcal{F}$, where $f_X^*(x)$ maximises the differential entropy $h\left(X^*\right)$, the right hand side of (5.1.13) is maximised and therefore, a tight lower bound is achieved [61]. By considering the constraint in (5.1.3), it can be proven that a uniformly distribution on X is the maximum entropy distribution.

$$X \sim \mathcal{U}\left(-\frac{A}{2}, \frac{A}{2}\right), \qquad (5.1.14)$$

$$h\left(X\right) = \log\left(A\right). \qquad (5.1.15)$$

The differential entropy $h\left(X\right)$ is then substituted into (5.1.13), resulting in the lower bound as

$$C \geq \frac{1}{2}\log\left(1 + \frac{2^{2\log(A)}}{2\pi e\sigma^2}\right), \qquad (5.1.16)$$

67
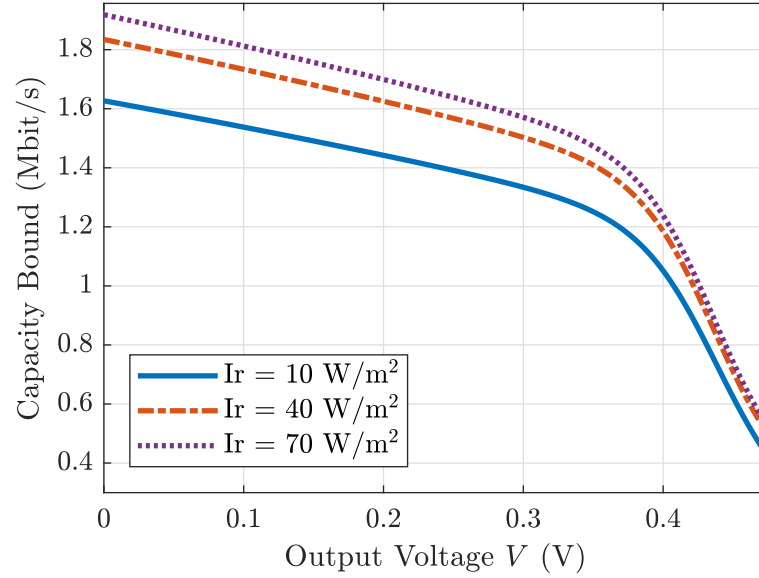
Figure 5.1: Channel capacity bound as a function of V ($\alpha = 0.1$).

$$C \geq \frac{1}{2} \log \left(1 + \frac{A^2}{2\pi e \sigma^2} \right). \tag{5.1.17}$$

As it was shown in Sec. 4.1.2, the receiver is bandwidth is limited to B(V), and hence, the lower bound for the supported data rate, R is given by

$$R \geq B(V) \log \left(1 + \frac{A^2}{2\pi e B(V) N_0} \right). \tag{5.1.18}$$

From Sec. 2.3.1, the lower bound is written in terms of current I as

$$C \geq B(V) \log \left(1 + \frac{(\alpha I)^2}{B(V) N_0} c_0 \right) \quad [\text{bits/s}],$$
$$c_0 = \frac{1}{2\pi e}. \tag{5.1.19}$$

5.2   Power-Rate Trade-off

Fig. 5.1. shows the variation of the supported rate with V at different irradiance levels (with $\alpha = 0.1$ in all simulations). Note that the supported rate increases as the irradiance increases, since the magnitude of the output current increases with the irradiance while the bandwidth remains constant.
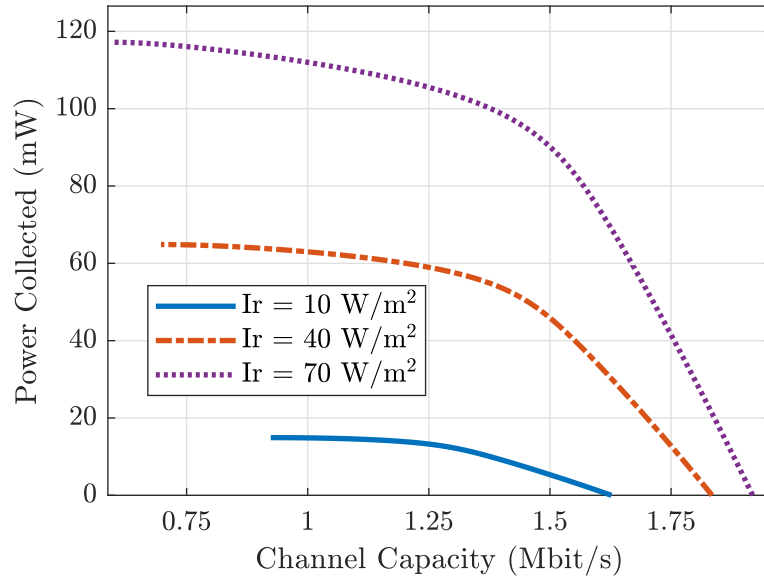
Figure 5.2: P-R characteristics ($\alpha = 0.1$) for different irradiance levels.

Note also that the interval of interest is $V \in (0, V_{mpp}]$ given that both the harvested power and supported rate decrease when the operating voltage increases beyond V_{mpp}. Condition (5.3.1b) is to ensure that we are operating the photo-voltaic region to produce power, and (5.3.1c) is to ensure that we do not exceed the region where both power and rate are reduced.

Figure 5.2 illustrates the power versus rate (P-R) characteristics for a solar cell adaptive-SLIPT receiver over a variety of irradiance levels.

Note that for a given irradiance, the maximum power is harvested at $V = V_{mpp}$
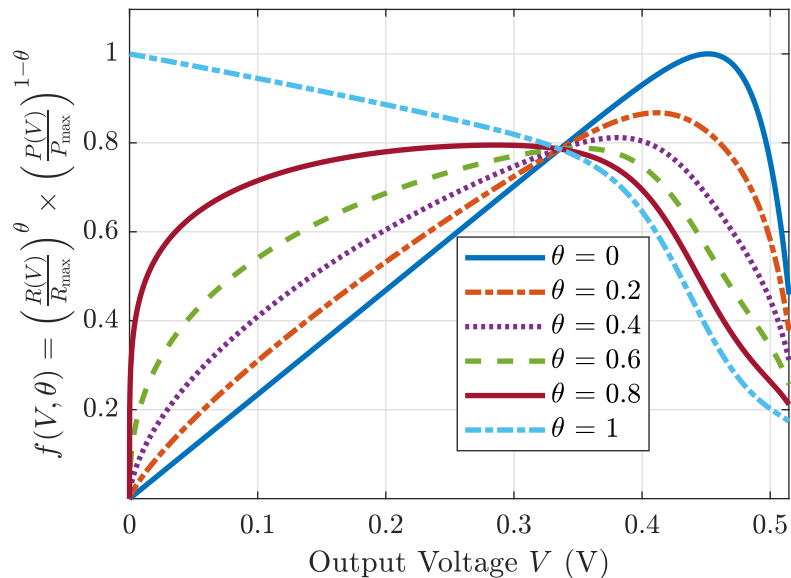
Figure 5.3: Geometric mean for different values of θ for an irradiance of $\mathrm{Ir} = 40 \ \mathrm{W/m^2}$.

corresponding to the minimum data rate. The system achieves a higher data rate by reducing V, at the expense of reduced collected power P. In addition, as irradiance reduces, the range of available P and R also reduce.

5.3 System Design

Depending on the requirements, power harvesting may need to be prioritised over data rate or vice versa. Thus, a system design must be performed to select the optimum operating voltage, V^*, of the solar cell-based receiver.

Consider selecting $V = V^*$ to optimise the weighted geometric mean of R and P

(which is especially appropriate given their different scales). In particular,

$$\textbf{(P1)} \quad \max_{V^*} \quad \left(\frac{R(V)}{R_{\max}}\right)^{\theta} \times \left(\frac{P(V)}{P_{\max}}\right)^{1-\theta}, \tag{5.3.1a}$$

$$\text{subject to} \quad V > 0, \tag{5.3.1b}$$

$$V \leq V_{mpp}. \tag{5.3.1c}$$

where $\theta \in [0, 1]$ is the battery charge state and R_{max} and P_{max} correspond to the maximum data rate and power, respectively. The value of θ determines whether the data rate is prioritised over the power or vice verse. Depending on requirements, such as battery charge state or data queue length, the value of θ is chosen. For example, $\theta = 0$ maximises the power collected only, neglecting data rate and can be chosen when the battery level is critically low. Whereas $\theta = 1$ maximises the data rate only and neglects the power collected; an appropriate choice for a fully charged battery.

Another objective that could also be considered is the arithmetic mean

$$\textbf{(P2)} \quad \max_{V^*} \quad \theta\left(\frac{R(V)}{R_{\max}}\right) + (1-\theta)\left(\frac{P(V)}{P_{\max}}\right), \tag{5.3.2a}$$

$$\text{subject to} \quad V > 0, \tag{5.3.2b}$$

$$V \leq V_{mpp}. \tag{5.3.2c}$$

Fig. 5.3 and Fig. 5.4 show plots of the geometric and arithmetic mean objectives, respectively. It is clear that each curve in Fig. 5.3 and Fig. 5.4 reaches a maximum and hence, yields a unique V^*. An interesting observation is that the plotted curves of both objectives cross each other at one point. At this point, the objectives become

71
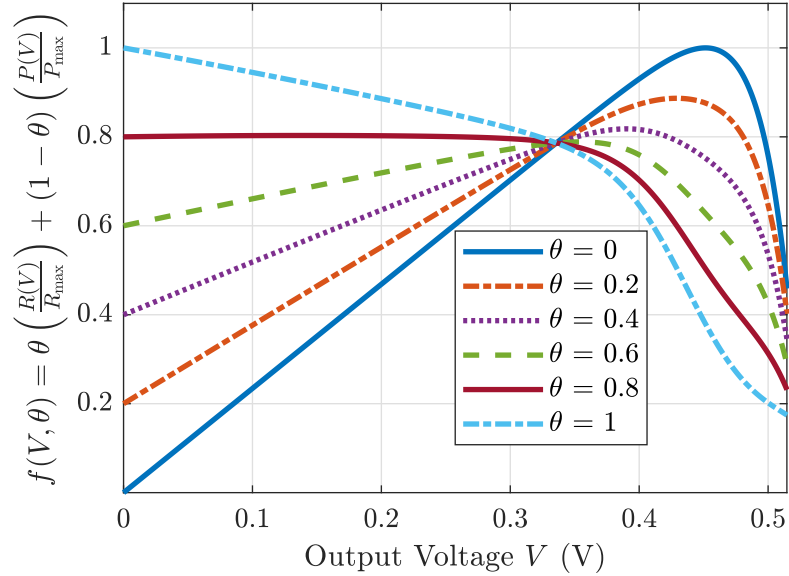
Figure 5.4: Arithmetic mean for different values of θ for an irradiance of $\mathrm{Ir} = 40 \ \mathrm{W/m^2}$.

independent of the battery state θ. This point is unique for each irradiance and exists when the condition in (5.3.3) holds true.

$$\left(\frac{P}{P_{\max}} \right) = \left(\frac{R}{R_{\max}} \right) \tag{5.3.3}$$

For both objective functions, the optimisation problem in (5.3.1a) and (5.3.2a) are non-convex and a closed-form solution for the optimum voltage is difficult to obtain. Hence, the optimal voltage, V^*, for both objectives were found through an exhaustive search for different values of θ and irradiance levels.

Although, the objective functions in (5.3.1a) and (5.3.2a) are non-convex, a unique maximum is attained for each value of θ. The numerically computed unique maxima, i.e., V^*, for different values of θ and irradiance levels are plotted in Fig. 5.5 and Fig. 5.6.

Figure 5.5: Optimal V^* as a function of battery charge state θ for the geometric mean objective.

Figure 5.6: Optimal V^* as a function of battery charge state θ for the arithmetic mean objective.
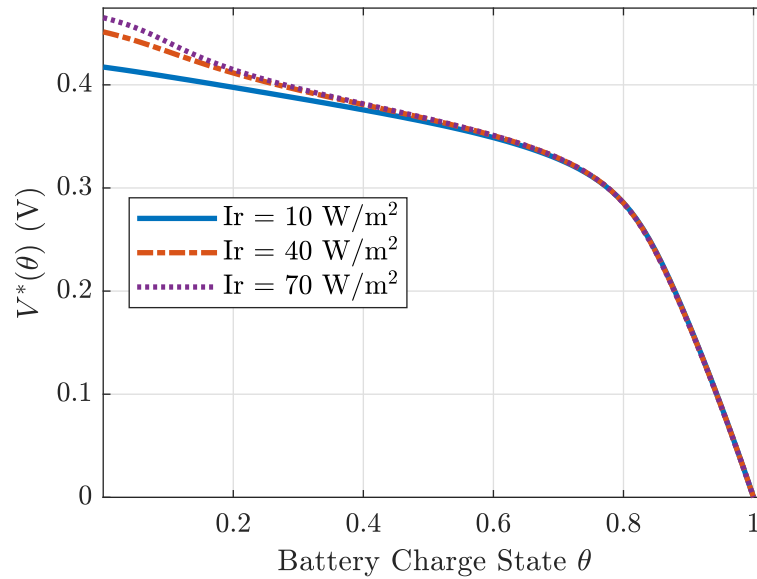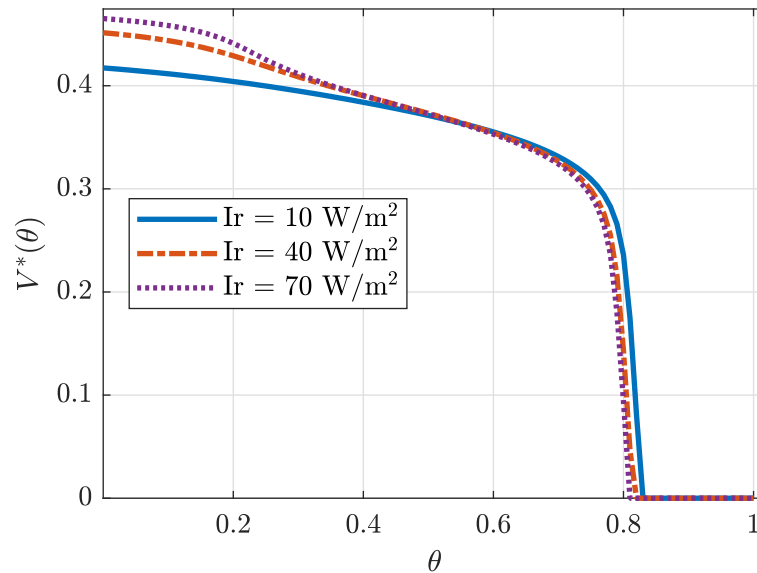
It is interesting to note that for the geometric objective for $\theta \geq 0.4$, the optimum voltage is approximately independent of the input irradiance level. For the arithmetic objective, the optimal voltage is entirely independent of the irradiance level and the battery state for $\theta \gtrapprox 0.82$. Both objectives yield the same optimal V^* for $\theta = 0$, $\theta = 0.5$ and $\theta = 1$.

The optimal P-R pairs, corresponding to the optimal V^* of the geometric and arithmetic mean objectives for $\theta \in \{0, 0.1, 0.2, 0.3, 0.4, 0.5, 0.6, 0.7, 0.8, 0.9, 1\}$ are indicated with solid markers in Fig. 5.7 and Fig. 5.8, respectively. By inspecting the two figures, we find that for the geometric mean objective in Fig. 5.7, the optimal P-R pairs are more evenly distributed with respect to θ compared to Fig. 5.8 with the arithmetic mean objective. This also indicates that the geometric mean objective is better suited for this system since it would allow for a smooth trade-off between the rate and power. In addition, given the scale difference in power ($\approx 10^{-3}$) and rate ($\approx 10^6$), for the arithmetic mean objective, these quantities must be normalised using P_{max} and R_{max} as shown in 5.3.2a. These values are not required for the geometric objective since the multiplicative product does not require to be normalised.

By observing the plots in Fig. 5.5 and Fig. 5.6, it is readily apparent that setting $V = V_{mpp}$ is not necessarily the optimum operating voltage when visible light communication is prioritised. Depending on the battery charge state, communication constraints and irradiance levels, an optimum operating voltage can be chosen based on the results presented above. In practice, these optimum voltages can be computed offline, and a look-up table can be employed at the receiver to choose the optimum operating voltage depending on the requirements.

In addition, if an implementation of the adaptive-SLIPT receiver is not feasible

Figure 5.7: The markers indicate the P-R pairs corresponding to the optimal operating voltage, V^* for the geometric objective at different battery states θ.

for a given device, the best stationary operation point would be one for which the objectives are maximum for $\theta = \frac{1}{2}$ which is the mid-point for $\theta \in [0, 1]$.

5.4   Conclusions

In this chapter, a tight upper bound for the capacity of the designed receiver was derived. It was found that the supported data rate of the receiver is dependant on the DC operating voltage of the solar cell as well as the irradiance level. The derived lower bound was then used to plot and quantify the trade-off between the received power and the supported rate. It was found that one has to trade-off the rate of communication for power and vice-versa by controlling the DC operating voltage of the solar cell as opposed to the fixed DC operating voltage approach in the previous literature.
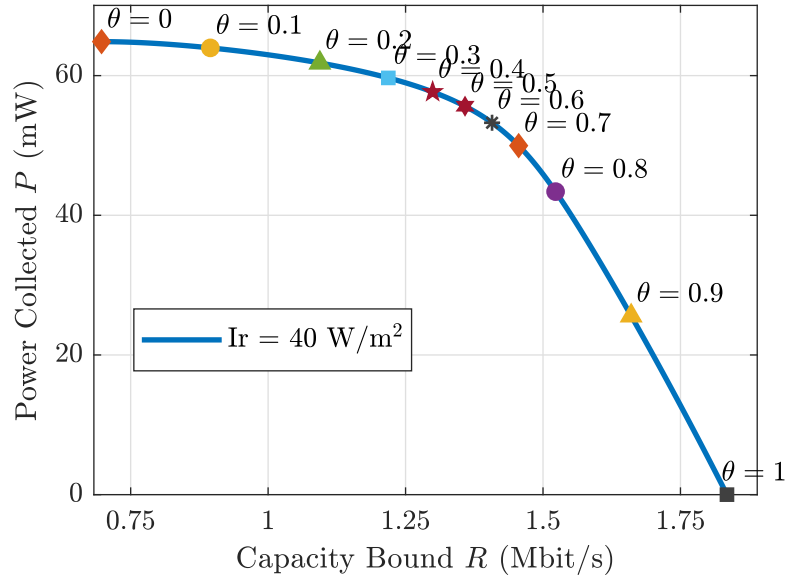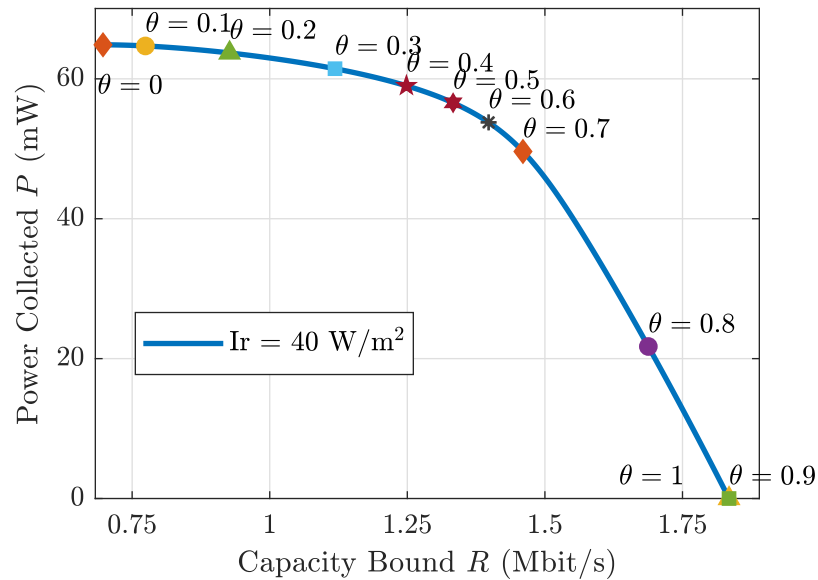
Figure 5.8: The markers indicate the P-R pairs corresponding to the optimal operating voltage, V^* for the arithmetic objective at different battery states θ.

Finally, a system design problem was formulated as an optimisation to find the optimum solar cell DC operating voltage to obtain a trade-off between rate R and power P for a given battery charge state θ and background irradiance. It was shown that the optimal voltage V^* changes with different values of θ.

Chapter 6

Conclusions

This thesis presents a novel solar cell-based adaptive-SLIPT receiver that enables a rate-power trade-off to be tuned for different battery charge states and illumination levels. The downside of the previously proposed solar cell-based receivers is in that the bandwidth is assumed to be constant in the previous designs, while the power is variant.

The main contribution of this thesis is the quantification the inherent rate-power trade-off in the solar cell-based receivers to show that in order to collect more power, the rate of communication is sacrificed and similarly, the maximum rate is achieved at the expense of having no DC power collection. The designed receiver offers an adaptive approach to the altering power and rate requirements of the device at any given time. Whereas, in the previous designs, the rate and power requirements would be addressed by adjustments made to the transmitted signal, which could potentially result in unwanted changes in the illumination of the indoor environment.

By expressing the electrical bandwidth of the receiver in terms of the DC operating point, the bandwidth was shown to vary significantly with the DC operating

point. Using the obtained expression for the bandwidth, a lower bound on the voltage dependant channel capacity of the system was derived in Chapter 4. The main contributor to the voltage dependency of the supported rate was shown to be the diffusion and depletion capacitances within the pn junction.

Both the supported data rate and collected power are dependant on the selection of the DC operating point of the solar cell by the DC-DC converter. This approach enables a more efficient SLIPT receiver design for indoor IoT scenarios which can adaptively prioritise power collection or data rate as necessary.

6.1   Future Work

As it was mentioned in the introduction, the main challenge involved with SLIPT systems is the fact that solar cells are built with one objective: To maximise output power. Hence, their small-signal characteristics are not in favour of detection of alternating power at a very high rate. The following potential future works aim to optimise the usage of solar cells for communications purposes.

6.1.1   Solar Panels

The work presented in this thesis considers a single solar cell. On the other hand, solar panels consist of N_s solar cells connected in series in order to produce a high output voltage. Some parallel connections are also made to increase the output current. A possible extension of this work would be to derive an equivalent small-signal model for a network of solar cells connected in series and parallel. Having this model would imply an expression for the electrical bandwidth of the solar panel, which would

enable a more realistic deployment of off-the-shelf solar panels for SLIPT receivers.

6.1.2   Solar Cell Area Optimisation

One of the most critical parameters that determine the potential amount of collectable power a solar cell is its area A. Doubling the area ideally results in doubling the amount of power incident at the solar cell, hence leading to an increase in the amount of collectable power. On the other hand, according to the equations (3.7.1) and (3.7.2), increasing the area implies an increase in the capacitance of the solar cell. Another possible extension of this work could be to formulate a design problem in which the objective is to minimise the solar cell area A subject to constraints on the achievable rate and power collected. Minimising the solar cell area would enable smaller and cheaper IoT devices to be designed.

6.1.3   Multi-junction

As it was mentioned in Chapter 3, the Shockley-Queisser limit on the efficiency of the solar cell motivates research in multi-junction solar cells. Multi-junction solar cells consist of n junctions, each of a different semiconductor. This type of solar cells offer the highest efficiency among all solar cells; hence, there is an incentive to analyse and derive a model of the multi-junction cell and examine the possibility deploying such cells as a multi-wavelength receiver in the future. Furthermore, another design problem could be defined as finding the minimal number of junctions n for a multi-junction solar cell, subject to bandwidth and output power constraints.

6.1.4   Experimental Demonstration

The majority of the literature for SLIPT is based on numerical simulations of a solar cell-based receiver. The solar cell characteristics in an experimental set up are likely to differ to that of a simulated solar cell. Hence, in order to discover the practical limitations of SLIPT systems, an experimental demonstration is essential. The experimental demonstration of the SLIPT receiver introduced in this work would involve setting up a VLC testbed equipped with a solar cell-based receiver and an LED luminaire in a LOS configuration.

Bibliography

[1] P. Kamalinejad, C. Mahapatra, Z. Sheng, S. Mirabbasi, V. C. Leung, and Y. L. Guan, "Wireless energy harvesting for the Internet of Things," *IEEE Communications Magazine*, vol. 53, no. 6, pp. 102–108, 2015.

[2] P. D. Diamantoulakis, G. K. Karagiannidis, and Z. Ding, "Simultaneous lightwave information and power transfer (SLIPT)," *IEEE Transactions on Green Communications and Networking*, vol. 2, no. 3, pp. 764–773, 2018.

[3] P. H. Pathak, X. Feng, P. Hu, and P. Mohapatra, "Visible light communication, networking, and sensing: A survey, potential and challenges," *IEEE Communications Surveys & Tutorials*, vol. 17, no. 4, pp. 2047–2077, 2015.

[4] L. E. M. Matheus, A. B. Vieira, L. F. Vieira, M. A. Vieira, and O. Gnawali, "Visible light communication: concepts, applications and challenges," *IEEE Communications Surveys & Tutorials*, vol. 21, no. 4, pp. 3204–3237, 2019.

[5] A. Al-Kinani, C.-X. Wang, L. Zhou, and W. Zhang, "Optical wireless communication channel measurements and models," *IEEE Communications Surveys & Tutorials*, vol. 20, no. 3, pp. 1939–1962, 2018.

[6] D. Karunatilaka, F. Zafar, V. Kalavally, and R. Parthiban, "LED based indoor visible light communications: State of the art," *IEEE Communications Surveys & Tutorials*, vol. 17, no. 3, pp. 1649–1678, 2015.

[7] C. Elliott, "Energy savings forecast of solid-state lighting in general illumination applications," *United States Department of Energy*, 12 2019. [Online]. Available: https://www.energy.gov/sites/prod/files/2020/02/f72/2019_ssl-energy-savings-forecast.pdf

[8] W. Pawlikowski, M. Narimani, and S. Hranilovic, "A novel method of integrating visible light communications within LED drivers," in *2017 IEEE Globecom Workshops (GC Wkshps)*. IEEE, 2017, pp. 1–6.

[9] L. Grobe, A. Paraskevopoulos, J. Hilt, D. Schulz, F. Lassak, F. Hartlieb, C. Kottke, V. Jungnickel, and K.-D. Langer, "High-speed visible light communication systems," *IEEE Communications Cagazine*, vol. 51, no. 12, pp. 60–66, 2013.

[10] A. A. Purwita and H. Haas, "IQ-WDM for IEEE 802.11bb-based LiFi," in *2020 IEEE Wireless Communications and Networking Conference (WCNC)*, 2020, pp. 1–6.

[11] "Home - pureLiFi - connectivity is evolving." [Online]. Available: https://purelifi.com/

[12] "Home." [Online]. Available: https://www.signify.com/global

[13] "Light Fidelity (LiFi) internet service provider company." [Online]. Available: https://www.oledcomm.net/

[14] "VLNComm – LiFi at its best." [Online]. Available: https://vlncomm.com/

[15] T.-H. Do and M. Yoo, "An in-depth survey of visible light communication based positioning systems," *Sensors*, vol. 16, no. 5, p. 678, 2016.

[16] C. Wang, L. Wang, X. Chi, S. Liu, W. Shi, and J. Deng, "The research of indoor positioning based on visible light communication," *China Communications*, vol. 12, no. 8, pp. 85–92, 2015.

[17] S. Yang, E. Jung, and S. Han, "Indoor location estimation based on LED visible light communication using multiple optical receivers," *IEEE Communications Letters*, vol. 17, no. 9, pp. 1834–1837, 2013.

[18] A. Arafa, S. Dalmiya, R. Klukas, and J. F. Holzman, "Angle-of-arrival reception for optical wireless location technology," *Optics express*, vol. 23, no. 6, pp. 7755–7766, 2015.

[19] K. Majeed and S. Hranilovic, "Passive indoor localization for visible light communication systems," in *2018 IEEE Global Communications Conference (GLOBE-COM)*.   IEEE, 2018, pp. 1–6.

[20] K. Majeed and S. Hranilovic, "Performance bounds on passive indoor positioning using visible light," *Journal of Lightwave Technology*, vol. 38, no. 8, pp. 2190–2200, 2020.

[21] A. Ganick and D. Ryan, "Method and system for determining the position of a device in a light based positioning system using locally stored maps," Mar. 31 2015, uS Patent 8,994,799.

[22] M. Wright, "Acuity acquires indoor-location-services specialist ByteLight," *LEDs Magazine*, Apr 2015. [Online]. Available: https://www.ledsmagazine.com/architectural-lighting/retail-hospitality/article/16696795/acuity-acquires-indoorlocationservices-specialist-bytelight

[23] "Atrius Navigator - Atrius Navigator indoor positioning and location-based platform service SDK." [Online]. Available: https://www.acuitybrands.com/products/detail/776333/atrius/atrius-navigator/atrius-navigator-indoor-positioning-and-location-based-platform-service-sdk

[24] "LED based indoor positioning." [Online]. Available: https://www.usa.lighting.philips.com/systems/lighting-systems/indoor-positioning

[25] "Indoor navigation." [Online]. Available: https://images.philips.com/is/content/PhilipsConsumer/PDFDownloads/UnitedStates/ODLI20180904_001-UPD-en_US-INt-1803FL.pdf

[26] I. Marin-Garcia, V. Guerra, P. Chavez-Burbano, J. Rabadan, and R. Perez-Jimenez, "Evaluating the risk of eavesdropping a visible light communication channel," *IET Optoelectronics*, vol. 12, no. 6, pp. 289–292, 2018.

[27] "Visible light for broadband communications," Jun 2019. [Online]. Available: https://www.itu.int/dms_pub/itu-r/opb/rep/R-REP-SM.2422-1-2019-PDF-E.pdf

[28] H. Kaushal and G. Kaddoum, "Underwater optical wireless communication," *IEEE access*, vol. 4, pp. 1518–1547, 2016.

[29] N. Anous, M. Abdallah, M. Uysal, and K. Qaraqe, "Performance evaluation of los and nlos vertical inhomogeneous links in underwater visible light communications," *IEEE Access*, vol. 6, pp. 22 408–22 420, 2018.

[30] "BlueComm 100 - wireless underwater optical communication," Jul 2020. [Online]. Available: https://www.sonardyne.com/product/bluecomm-underwater-optical-communication-system/

[31] Y. Qiao, Z. Xia, X. Hong, and J. Shen, "A visible light communication based vehicle collision avoidance scheme for curve lane situations," in *2017 9th International Conference on Advanced Infocomm Technology (ICAIT)*.   IEEE, 2017, pp. 214–217.

[32] M. Boban, A. Kousaridas, K. Manolakis, J. Eichinger, and W. Xu, "Connected roads of the future: Use cases, requirements, and design considerations for vehicle-to-everything communications," *IEEE Vehicular Vechnology Vagazine*, vol. 13, no. 3, pp. 110–123, 2018.

[33] S. Sudevalayam and P. Kulkarni, "Energy harvesting sensor nodes: Survey and implications," *IEEE Communications Surveys & Tutorials*, vol. 13, no. 3, pp. 443–461, 2010.

[34] J. A. Paradiso and T. Starner, "Energy scavenging for mobile and wireless electronics," *IEEE Pervasive Computing*, vol. 4, no. 1, pp. 18–27, 2005.

[35] D. Wilson, *Wearable Solar Cell Systems*.   CRC Press, 2019.

[36] S. Kim, R. Vyas, J. Bito, K. Niotaki, A. Collado, A. Georgiadis, and M. M. Tentzeris, "Ambient RF energy-harvesting technologies for self-sustainable standalone wireless sensor platforms," *Proceedings of the IEEE*, vol. 102, no. 11, pp. 1649–1666, 2014.

[37] M. Shirvanimoghaddam, K. Shirvanimoghaddam, M. M. Abolhasani, M. Farhangi, V. Z. Barsari, H. Liu, M. Dohler, and M. Naebe, "Paving the path to a green and self-powered Internet of Things," *arXiv preprint arXiv:1712.02277*, 2017.

[38] D. W. K. Ng, T. Q. Duong, C. Zhong, and R. Schober, *Wireless Information and Power Transfer: Theory and Practice.* John Wiley & Sons, 2019.

[39] N. Shinohara, *Wireless Power Transfer: Theory, technology, and applications.* Institution of Engineering & Technology, 2018.

[40] C. R. Valenta and G. D. Durgin, "Harvesting wireless power: Survey of energy-harvester conversion efficiency in far-field, wireless power transfer systems," *IEEE Microwave Magazine*, vol. 15, no. 4, pp. 108–120, 2014.

[41] O. Cetinkaya and O. B. Akan, "Electric-field energy harvesting in wireless networks," *IEEE Wireless Communications*, vol. 24, no. 2, pp. 34–41, 2017.

[42] L. Wheeler, "II—Tesla's contribution to high frequency," *Electrical Engineering*, vol. 62, no. 8, pp. 355–357, 1943.

[43] X. Lu, P. Wang, D. Niyato, D. I. Kim, and Z. Han, "Wireless networks with RF energy harvesting: A contemporary survey," *IEEE Communications Surveys & Tutorials*, vol. 17, no. 2, pp. 757–789, 2014.

[44] N. Shinohara, "Power without wires," *IEEE Microwave Magazine*, vol. 12, no. 7, pp. S64–S73, 2011.

[45] "Wi-Charge's long-range wireless power products earn UL certification - Wi-Charge," Dec 2019. [Online]. Available: https://wi-charge.com/wi-charges-long-range-wireless-power-products-earn-ul-certification/

[46] P. D. Diamantoulakis, "Resource allocation in wireless networks with energy constraints," Ph.D. dissertation, Aristotle University of Thessaloniki School of Electrical and Computer Engineering Telecommunications Department, Sep 2017. [Online]. Available: https://ikee.lib.auth.gr/record/295341/files/GRI-2017-20727.pdf

[47] T. D. P. Perera, D. N. K. Jayakody, S. K. Sharma, S. Chatzinotas, and J. Li, "Simultaneous wireless information and power transfer (SWIPT): Recent advances and future challenges," *IEEE Communications Surveys & Tutorials*, vol. 20, no. 1, pp. 264–302, 2017.

[48] S. A. Tegos, P. D. Diamantoulakis, K. N. Pappi, P. C. Sofotasios, S. Muhaidat, and G. K. Karagiannidis, "Toward efficient integration of information and energy reception," *IEEE Transactions on Communications*, vol. 67, no. 9, pp. 6572–6585, 2019.

[49] S. A. Tegos, P. D. Diamantoulakis, K. Pappi, and G. K. Karagiannidis, "Optimal simultaneous wireless information and power transfer with low-complexity receivers," in *2018 IEEE 19th International Workshop on Signal Processing Advances in Wireless Communications (SPAWC)*.   IEEE, 2018, pp. 1–5.

[50] P. D. Diamantoulakis and G. K. Karagiannidis, "Simultaneous lightwave information and power transfer (SLIPT) for indoor IoT applications," in *GLOBE-COM 2017-2017 IEEE Global Communications Conference*.   IEEE, 2017, pp. 1–6.

[51] S. O. Saltsman, "The silicon solar cell as an optical detector," Master's thesis, Florida Technological University, 1977.

[52] Z. Wang, D. Tsonev, S. Videv, and H. Haas, "On the design of a solar-panel receiver for optical wireless communications with simultaneous energy harvesting," *IEEE Journal on Selected Areas in Communications*, vol. 33, no. 8, pp. 1612–1623, 2015.

[53] M. Obeed, H. Dahrouj, A. M. Salhab, S. A. Zummo, and M.-S. Alouini, "DC-bias and power allocation in cooperative VLC networks for joint information and energy transfer," *IEEE Transactions on Wireless Communications*, vol. 18, no. 12, pp. 5486–5499, 2019.

[54] A. M. Abdelhady, O. Amin, A. Chaaban, and M.-S. Alouini, "Resource allocation for outdoor visible light communications with energy harvesting capabilities," in *2017 IEEE Globecom Workshops (GC Wkshps)*.   IEEE, 2017, pp. 1–6.

[55] A. M. Abdelhady, O. Amin, A. Chaaban, B. Shihada, and M.-S. Alouini, "Spectral-efficiency—illumination Pareto front for energy harvesting enabled VLC systems," *IEEE Transactions on Communications*, vol. 67, no. 12, pp. 8557–8572, 2019.

[56] S. Das, E. Poves, J. Fakidis, A. Sparks, S. Videv, and H. Haas, "Towards energy neutral wireless communications: Photovoltaic cells to connect remote areas," *Energies*, vol. 12, no. 19, p. 3772, 2019.

[57] M. Obeed, A. M. Salhab, M.-S. Alouini, and S. A. Zummo, "On optimizing VLC networks for downlink multi-user transmission: A survey," *IEEE Communications Surveys & Tutorials*, vol. 21, no. 3, pp. 2947–2976, 2019.

[58] S. Sepehrvand, L. N. Theagarajan, and S. Hranilovic, "Rate-power trade-off in simultaneous lightwave information and power transfer systems," *Submitted to IEEE Wireless Communication Letters*, 2020.

[59] Z. Ghassemlooy, W. Popoola, and S. Rajbhandari, *Optical Wireless Communications: System and Channel Modelling with MATLAB®*.   CRC press, 2019.

[60] J. M. Kahn and J. R. Barry, "Wireless infrared communications," *Proceedings of the IEEE*, vol. 85, no. 2, pp. 265–298, 1997.

[61] S. Hranilovic, *Wireless Optical Communication Systems*.   Springer Science & Business Media, 2006.

[62] S. Kasap, *Optoelectronics & Photonics:Principles & Practices: International Edition*.   Pearson Education Limited, 2013. [Online]. Available: https://books.google.ca/books?id=Qp2pBwAAQBAJ

[63] "White lighting LEDs part number: Eahe2835wd03," 2015. [Online]. Available: https://everlightamericas.com/white-lighting-leds/2086/EAHE2835WD03.html

[64] H. Zhang, P. Liu, Q. Li, J. Liu, and S. Liu, "LED nonlinearity impact on frequency modulation signals over visible light communication systems," in *2015*

IEEE International Conference on Communication Problem-Solving (ICCP). IEEE, 2015, pp. 369–372.

[65] Z. Wang, Q. Wang, W. Huang, and Z. Xu, *Visible Light Communications: Modulation and Signal Processing.* John Wiley & Sons, 2017.

[66] R. Lenk and C. Lenk, *Practical lighting design with LEDs.* John Wiley & Sons, 2017.

[67] D. Zhu and C. J. Humphreys, "Solid-state lighting based on light emitting diode technology," in *Optics In Our Time.* Springer, Cham, 2016, pp. 87–118.

[68] M. D. Al-Amri, M. El-Gomati, and M. Suhail Zubairy, *Optics in Our Time.* Springer Nature, 2016.

[69] "LUXEON FlipChip White 05," Jul 2020. [Online]. Available: https://www.lumileds.com/wp-content/uploads/files/DS174-luxeon-5050-datasheet.pdf

[70] S. O. Kasap, *Optoelectronics and photonics.* Prentice Hall, 2001.

[71] S. Zhang, D. Tsonev, S. Videv, S. Ghosh, G. A. Turnbull, I. D. Samuel, and H. Haas, "Organic solar cells as high-speed data detectors for visible light communication," *Optica*, vol. 2, no. 7, pp. 607–610, 2015.

[72] Z. Ghassemlooy, W. Popoola, and S. Rajbhandari, "Optical wireless communications: System and channel modelling with MATLAB," 2012.

[73] T. Komine and M. Nakagawa, "Fundamental analysis for visible-light communication system using LED lights," *IEEE Transactions on Consumer Electronics*, vol. 50, no. 1, pp. 100–107, 2004.

[74] J. Nelson, *The Physics of Solar Cells.* World Scientific Publishing Company, 2003.

[75] *MATLAB version 9.5.0.944444 (R2018b)*, The Mathworks, Inc., Natick, Massachusetts, 2018.

[76] H. Häberlin, *Photovoltaics: System Design and Practice.* John Wiley & Sons, 2012.

[77] A. Jain and A. Kapoor, "Exact analytical solutions of the parameters of real solar cells using Lambert W-function," *Solar Energy Materials and Solar Cells*, vol. 81, no. 2, pp. 269–277, 2004.

[78] T. Esram and P. L. Chapman, "Comparison of photovoltaic array maximum power point tracking techniques," *IEEE Transactions on Energy Conversion*, vol. 22, no. 2, pp. 439–449, 2007.

[79] A. R. Jha, *Solar Cell Technology and Applications.* CRC press, 2009.

[80] A. Willoughby, *Solar Cell Materials: Developing technologies.* John Wiley & Sons, 2014.

[81] M. A. Green, E. D. Dunlop, D. H. Levi, J. Hohl-Ebinger, M. Yoshita, and A. W. Ho-Baillie, "Solar cell efficiency tables (version 54)," *Progress in photovoltaics: research and applications*, vol. 27, no. 7, pp. 565–575, 2019.

[82] J.-F. Guillemoles, T. Kirchartz, D. Cahen, and U. Rau, "Guide for the perplexed to the Shockley–Queisser model for solar cells," *Nature Photonics*, vol. 13, no. 8, pp. 501–505, 2019.

[83] A. Polman, M. Knight, E. C. Garnett, B. Ehrler, and W. C. Sinke, "Photovoltaic materials: Present efficiencies and future challenges," *Science*, vol. 352, no. 6283, 2016.

[84] W. Shockley and H. J. Queisser, "Detailed balance limit of efficiency of p-n junction solar cells," *Journal of applied physics*, vol. 32, no. 3, pp. 510–519, 1961.

[85] M. A. Green, "Third generation photovoltaics: solar cells for 2020 and beyond," *Physica E: Low-dimensional Systems and Nanostructures*, vol. 14, no. 1-2, pp. 65–70, 2002.

[86] A. De Vos, "Detailed balance limit of the efficiency of tandem solar cells," *Journal of Physics D: Applied Physics*, vol. 13, no. 5, p. 839, 1980.

[87] B. Zhao, C. Wang, and X. Zhang, "Grid-integrated and standalone photovoltaic distributed generation systems," *Analysis, Design, and Control. Wiley*, 2017.

[88] E. Koutroulis and F. Blaabjerg, "Overview of maximum power point tracking techniques for photovoltaic energy production systems," *Electric Power Components and Systems*, vol. 43, no. 12, pp. 1329–1351, 2015.

[89] N. Femia, G. Petrone, G. Spagnuolo, and M. Vitelli, "Optimization of perturb and observe maximum power point tracking method," *IEEE Transactions on Power Electronics*, vol. 20, no. 4, pp. 963–973, 2005.

[90] J. J. Nedumgatt, K. B. Jayakrishnan, S. Umashankar, D. Vijayakumar, and D. P. Kothari, "Perturb and observe MPPT algorithm for solar PV systems-modeling and simulation," in *2011 Annual IEEE India Conference*, 2011, pp. 1–6.

[91] L. A. Mallette, "Modeling the silicon solar cell as an optical detector," Master's thesis, Florida Technological University, 1977.

[92] S. O. Kasap, *Principles of Electronic Materials and Devices*. Tata McGraw-Hill, 2006.

[93] J. Bisquert, *The Physics of Solar Energy Conversion: Perovskites, Organics, and Photovoltaic Fundamentals*. CRC Press, 2020.

[94] I. Mora-Sero, G. Garcia-Belmonte, P. P. Boix, M. A. Vazquez, and J. Bisquert, "Impedance spectroscopy characterisation of highly efficient silicon solar cells under different light illumination intensities," *Energy & Environmental Science*, vol. 2, no. 6, pp. 678–686, 2009.

[95] D. W. Hart, *Power Electronics*. Tata McGraw-Hill Education, 2011.

[96] A. S. Weddell, G. V. Merrett, and B. M. Al-Hashimi, "Ultra low-power photovoltaic MPPT technique for indoor and outdoor wireless sensor nodes," in *2011 Design, Automation & Test in Europe*. IEEE, 2011, pp. 1–4.

[97] T. M. Cover and J. A. Thomas, *Elements of Information Theory*. John Wiley & Sons, 2012.

[98] A. Lapidoth, S. M. Moser, and M. A. Wigger, "On the capacity of free-space optical intensity channels," *IEEE Transactions on Information Theory*, vol. 55, no. 10, pp. 4449–4461, 2009.